

Dynamical Mass of the Exoplanet Host Star HR 8799

ALDO G. SEPULVEDA^{1, 2, 3, *} AND BRENDAN P. BOWLER³

¹ Institute for Astronomy, University of Hawai'i at Mānoa, 2680 Woodlawn Drive, Honolulu, HI 96822, USA

² Department of Physics & Astronomy, The University of Texas at San Antonio, 1 UTSA Circle San Antonio, TX, 78249, USA

³ Department of Astronomy, The University of Texas at Austin, 2515 Speedway Blvd. Stop C1400 Austin, TX 78712, USA

ABSTRACT

HR 8799 is a young A5/F0 star hosting four directly imaged giant planets at wide separations (\sim 16–78 au) which are undergoing orbital motion and have been continuously monitored with adaptive optics imaging since their discovery over a decade ago. We present a dynamical mass of HR 8799 using 130 epochs of relative astrometry of its planets, which include both published measurements and new medium-band 3.1 μ m observations that we acquired with NIRC2 at Keck Observatory. For the purpose of measuring the host star mass, each orbiting planet is treated as a massless particle and is fit with a Keplerian orbit using Markov chain Monte Carlo. We then use a Bayesian framework to combine each independent total mass measurement into a cumulative dynamical mass using all four planets. The dynamical mass of HR 8799 is $1.47^{+0.12}_{-0.17}$ M_{\odot} assuming a uniform stellar mass prior, or $1.46^{+0.11}_{-0.15}$ M_{\odot} with a weakly informative prior based on spectroscopy. There is a strong covariance between the planets' eccentricities and the total system mass; when the constraint is limited to low eccentricity solutions of $e < 0.1$, which is motivated by dynamical stability, our mass measurement improves to $1.43^{+0.06}_{-0.07}$ M_{\odot} . Our dynamical mass and other fundamental measured parameters of HR 8799 together with MESA Isochrones & Stellar Tracks grids yields a bulk metallicity most consistent with $[\text{Fe}/\text{H}] \sim -0.25$ –0.00 dex and an age of 10–23 Myr for the system. This implies hot start masses of 2.7–4.9 M_{Jup} for HR 8799 b and 4.1–7.0 M_{Jup} for HR 8799 c, d, and e, assuming they formed at the same time as the host star.

Keywords: Astrometry (80) — Bayes' Theorem (1924) — Coronagraphic imaging (313) — Exoplanet systems (484) — Stellar ages (1581) — Stellar masses (1614)

1. INTRODUCTION

HR 8799 is a A5/F0 V star (Gray & Kaye 1999) that is most well known for hosting four exoplanets that have been directly imaged within a cold extended debris disk and beyond a warmer interior dust belt (Marois et al. 2008, 2010; Su et al. 2009; Booth et al. 2016; Wilner et al. 2018; Faramaz et al. 2021; see also review by Konopacky & Barman 2018). Among directly imaged systems, HR 8799 stands out as an unusual case of protoplanetary disk evolution due to its multiple planets orbiting at wide separations. In addition to HR 8799, the only other currently known systems with multiple imaged exoplanets are the young stars PDS 70, which hosts two accreting protoplanets within its transition

disk (Keppler et al. 2018; Haffert et al. 2019; Mesa et al. 2019), TYC 8998-760-1, which hosts two recently detected giant planets at wide separations (Bohn et al. 2020a,b), and β Pictoris, which harbors two giant planets orbiting within 10 au (Lagrange et al. 2009, 2010, 2019; Nowak et al. 2020). HR 8799 itself is also unusual with respect to other A stars: it is a λ Boötis star with a peculiar surface abundance pattern (Gray & Kaye 1999; Sadakane 2006; Moya et al. 2010b; Murphy et al. 2015) and a γ Dor pulsator (Rodriguez & Zerbi 1995; Zerbi et al. 1999; Kaye et al. 1999; Moya et al. 2010a). The stellar radius of HR 8799 has been directly measured (Baines et al. 2012); however, its mass, age, and bulk composition are either poorly constrained or inferred from models.

Continuous monitoring and “pre-discovery” observations of the HR 8799 planets have provided a baseline of over two decades of relative astrometry between the companions and host star. Prior studies have con-

Corresponding author: Aldo G. Sepulveda
 aldo.sepulveda@hawaii.edu

* NSF Graduate Research Fellow

strained the orbits of the companions (e.g., Soummer et al. 2011; Currie et al. 2012; Esposito et al. 2013; Goździewski & Migaszewski 2014; Pueyo et al. 2015; Maire et al. 2015; Zurlo et al. 2016; Konopacky et al. 2016; Wertz et al. 2017; Wang et al. 2018b; Gravity Collaboration et al. 2019), but the host star mass has been assumed to be fixed at $\sim 1.5 M_{\odot}$ in the majority of these analyses based on estimates from surface gravity measurements and high-mass evolutionary models (e.g., Gray & Kaye 1999; Moya et al. 2010a; Baines et al. 2012). For example, Maire et al. (2015), Zurlo et al. (2016) and Wertz et al. (2017) adopt a mass of $1.51 M_{\odot}$ based on the results of Baines et al. (2012), who inferred the mass by comparing their stellar radius measurement and effective temperature constraint to high-mass stellar evolution grids. Similarly, Konopacky et al. (2016) and Wang et al. (2018b) use a mass prior of $1.52 \pm 0.15 M_{\odot}$ for their orbit fitting analysis, which is also based on the results of Baines et al. (2012) coupled with an additional uncertainty to account for model systematics. Dynamical mass measurements, on the other hand, are “gold standards” because they rely only on Kepler’s laws (e.g., Hillenbrand & White 2004, see also review by Serenelli et al. 2021). While host star dynamical masses have been measured in other systems with a directly imaged substellar companion (e.g., β Pic, Nielsen et al. 2014; Wang et al. 2016; Dupuy et al. 2019; Gravity Collaboration et al. 2020; Nielsen et al. 2020; Lagrange et al. 2020; Vandal et al. 2020; Brandt et al. 2021a), it is more often the case that the modest orbital coverage from long-period planets cannot admit a well constrained dynamical mass (e.g., Bowler et al. 2020).

The precise age of HR 8799 remains unsettled but is important because it is necessary to infer mass estimates of the orbiting companions using substellar evolutionary models (e.g., Marley et al. 2007; Fortney et al. 2008; Marleau & Cumming 2014). If HR 8799 is a member of the Columba Association (Doyon et al. 2010; Zuckerman et al. 2011; Malo et al. 2013) then its age is 42^{+6}_{-4} Myr (Bell et al. 2015). However, Hinz et al. (2010) calculated the *UVW* space motion of HR 8799 using revised Hipparcos astrometry and called into question whether it is an unambiguous kinematic member of this group. They used their revised space motion together with modeling of the epicyclic orbit of HR 8799 and found that its distance from the center of Columba is implausibly large. Moya et al. (2010a) conducted an asteroseismic analysis of HR 8799 and estimated plausible ages as young as 26 Myr and as old as ~ 1.6 Gyr; however, their interpretation depends on the unknown inclination of the

host star¹. Faramaz et al. (2021) reevaluated the moving group membership status of HR 8799 by calculating the *UVW* space motion with the latest *Gaia* EDR3 astrometry (Gaia Collaboration et al. 2021) and using the BANYAN Σ tool (Gagné et al. 2018). When using the stellar radial velocity constraints derived from Wang et al. (2018a) and Ruffio et al. (2019), they found that HR 8799 is more likely to be a field star rather than a member of Columba. Brandt et al. (2021b) recently presented a dynamical mass for the planet HR 8799 e and used it to derive a hot-start cooling age of 42^{+24}_{-16} Myr.

In this study, we independently constrain the dynamical mass of HR 8799 by fitting orbits to relative astrometry of each of the four companions utilizing *all* previously published astrometry together with a new epoch we obtained of planets b, c, and d using Keck/NIRC2 in 2015. We then jointly derive the dynamical mass distribution of HR 8799 in a Bayesian framework by assuming the total mass interior to each orbit is simply the stellar mass ($M_{total} \approx M_{\star}$). HR 8799’s dynamical mass, measured radius, bolometric luminosity, and effective temperature together with high-mass stellar evolutionary models offer a way to determine the system age independent of kinematic constraints, which in turn can be used to refine the inferred masses of the four planets using substellar evolution models.

In §2 we describe our new observations of the outer three planets with Keck/NIRC2 and summarize the additional astrometry that we use in our analysis. We detail the orbit fitting procedure and our Bayesian framework to jointly constrain the host star mass in §3. Results are summarized in §4 and we explore the implications of our dynamical mass in §5.

2. OBSERVATIONS

2.1. New Keck/NIRC2 Astrometry

We observed HR 8799 on UT 2015 August 28 with the NIRC2 near-infrared camera coupled with natural guide star adaptive optics at Keck Observatory (Wizinowich 2013). The narrow camera mode was used, providing a plate scale of 9.971 ± 0.004 mas pix⁻¹ (Service et al. 2016) and a $10.^{\prime\prime}2 \times 10.^{\prime\prime}2$ field of view. To sample a bright region of the planets’ emergent spectrum and yield high Strehl ratios, thermal infrared observations were taken with the H_2O ice filter ($\lambda_{\text{central}} = 3.063 \mu\text{m}$;

¹ Wright et al. (2011) conducted a spectroscopic asteroseismic analysis and found the stellar inclination to be $i_{\star} \gtrsim 40^{\circ}$. However, asteroseismic studies of HR 8799 are generally difficult to carry out due in part to the complex nature of its pulsation frequencies (e.g., Sódar et al. 2014).

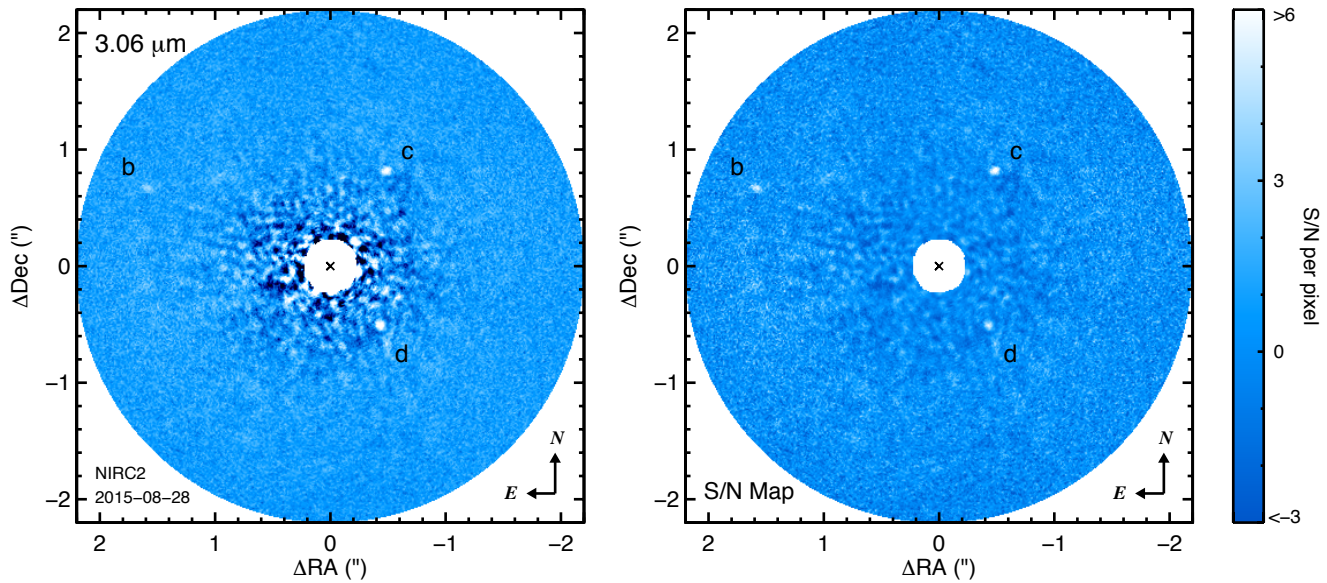


Figure 1. NIRC2 3- μ m observation of HR 8799. The left panel shows the processed (PSF-subtracted) image, revealing HR 8799 b, c, d. Planet e is not detected at a significant level in this dataset. The right panel shows the corresponding S/N map. North is up and east is to the left.

$\Delta\lambda = 0.155 \mu\text{m}$). A total of 119 images were acquired in pupil-tracking (ADI; Liu 2004; Marois et al. 2006) mode over the course of 2.1 hours with HR 8799 centered behind the 400 mas diameter partly-transparent Lyot coronagraph, amounting to a total field-of-view rotation of 185.5° . Each image has an integration time of 10 s and 3 coadds, totaling 3570 s (0.99 hr) of on-source integration time. Throughout transit, HR 8799 passes close to zenith at Mauna Kea so sky rotation is especially fast; during this time the sequence was interrupted for about 20 min during which time we obtained nearby 3 μm sky frames to serve as flats and 15 unsaturated images of the host star (each with an integration time of 0.1 s and 10 coadds) with the mask removed to photometrically calibrate the deeper coronagraphic dataset. Natural seeing in the visible (0.5 μm) ranged from $0''.5$ – $0''.6$ as recorded by the CFHT’s Differential Image Motion Monitor.

Bad pixels and cosmic rays were corrected using a nearest neighbor averaging algorithm, and each image was flat-fielded using a median-combined and normalized master sky frame. The bright sky background at 3 μm is removed by subtracting the master sky frame for each image. Images are registered following the description in Bowler et al. (2015); a 2D elliptical Gaussian is fit to the host star, which is visible behind the coronagraph, and an ADI data cube centered on HR 8799 is assembled. Each image is corrected for optical distortions with the distortion solution from Service et al. (2016). PSF subtraction is carried out using LOCI (Lafrenière et al.

2007) with the following parameter values that control the angular tolerance as well as optimization and subtraction zone sizes and shapes: $W=7$, $N_A=300$, $g=1.0$, $N_\delta=0.5$, and $dr=2.0$. Circular masks are placed at the locations of HR 8799 b, c, d, and e to avoid biasing the optimization regions during PSF subtraction.

The final processed image and signal-to-noise ratio (S/N) map are shown in Figure 1. Planets b, c, and d are clearly visible, but planet e is not evident at a significant level in the processed frame. S/Ns for each planet are computed using non-overlapping circular apertures of 6 pix at 36 azimuthal angles centered on HR 8799; we measure S/Ns of 9.8, 7.3, and 7.2 for planets b, c, and d, respectively. Astrometry and relative photometry for each source is calculated using the negative PSF injection approach described in Bowler et al. (2018). The median-combined unsaturated image of HR 8799 is used as the PSF model for each planet. The PSF model is inserted in the raw images with a starting guess position and (negative) amplitude. PSF subtraction is carried out in the same fashion as for our final processed image, and the RMS of the residuals at the location of the planet is used to assess the quality of subtraction. The amoeba downhill simplex algorithm (Nelder & Mead 1965) is used to find the best-fitting separation, P.A., and flux ratio of each planet (Figure 2). The uncertainties in these quantities are computed using the standard deviation of the last ten iterations of the amoeba algorithm as it settles in its final value that minimizes the

Table 1. Astrometric and photometric measurements from our NIRC2 observations.

Planet	UT Date	ρ (mas)	θ ($^{\circ}$)	ΔRA ($''$)	ΔDec ($''$)	Δmag
b	2015 Aug 28	1705 ± 12	67.0 ± 0.2	1.569 ± 0.011	0.666 ± 0.007	12.0 ± 0.5
c	2015 Aug 28	945 ± 7	329.3 ± 0.2	-0.482 ± 0.005	0.813 ± 0.006	10.9 ± 0.3
d	2015 Aug 28	671 ± 16	220.5 ± 0.3	-0.436 ± 0.011	-0.510 ± 0.012	10.9 ± 0.5

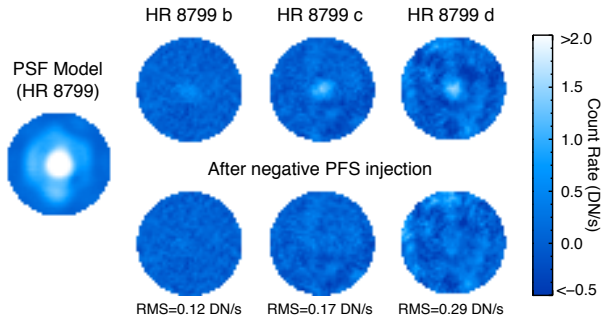


Figure 2. Cutouts showing our negative PSF injection strategy for astrometry and relative photometry. The unsaturated image of HR 8799 (left) is used as a PSF model. After optimizing the model position and amplitude, planets b, c, and d (top) are removed from the final processed image (bottom) while preserving the underlying noise structure.

RMS at a specified tolerance level. Based on results from Bowler et al. (2018), this method for estimating errors is comparable to values inferred by repeatedly injecting PSF templates into the raw data at various azimuthal angles and recovering them with the negative PSF injection approach. Results are reported in Table 1.

2.2. Previous Astrometry

We make use of all astrometry of the HR 8799 planets published prior to December 2020² in our orbit fitting analysis in addition to our new epoch from 2015. Observations of this system have been taken with a wide range of telescopes and instruments, including *HST*, Subaru, Keck, Gemini, MMT, VLT, Palomar, and LBT. Astrometry published prior to 2016 are presented in Bowler (2016, Table 4 in their Appendix)³. Additionally, we incorporate published astrometry obtained with Gem-

² During the course of this analysis, Biller et al. (2021) and Wahaj et al. (2021) presented new astrometry from VLT/SPHERE-IRDIS. While these data were not included in this study, continued astrometric monitoring will be essential for future studies of HR 8799.

³ We also include the 2010.55 and 2012.83 Keck/NIRC2 epochs presented in Currie et al. (2014), which were inadvertently omitted in the Bowler (2016) compilation.

ini/GPI (Wang et al. 2018b) and with VLTI/GRAVITY (Gravity Collaboration et al. 2019). For astrometry in ΔRA and ΔDec , we convert to separation and position angle and propagate the uncertainties in a Monte Carlo fashion. For multiple reductions of the same dataset, or where more than one dataset exists for the same epoch, we use the measurements that appear to have the most realistic astrometric errors. Specifically, for epoch 1998.83 we adopt astrometry from Soummer et al. (2011) over Lafrenière et al. (2009); Currie et al. (2011) over Hinz et al. (2010) for epochs 2008.89 and 2009.70; Currie et al. (2014) over Marois et al. (2010) for epoch 2010.55; Konopacky et al. (2016) over Marois et al. (2008), Metchev et al. (2009), Marois et al. (2010), Galicher et al. (2011), and Currie et al. (2012) for epochs 2007.58, 2007.81, 2008.72, 2009.58, 2009.83, 2010.53, and 2010.83, respectively; Wertz et al. (2017) over Zurlo et al. (2016) and Apai et al. (2016) for epoch 2014.93; and De Rosa et al. (2020) over Wang et al. (2018b) for epochs 2013.88, 2014.70, and 2016.72, respectively. Including our observations from 2015, this results in 35 epochs for planets b (1998.8–2015.7), 36 epochs for planets c (1998.8–2016.7), 35 epochs for planets d (1998.8–2016.7), and 24 epochs for planets e (2009.6–2018.7).

3. ORBIT FITS AND STATISTICAL FRAMEWORK

3.1. Accounting for Potential Systematic Errors

Using all available astrometry in the orbit fitting could introduce systematic errors from a variety of sources, including the use of differently calibrated instruments, PSF-subtraction algorithms, and strategies to measure relative astrometry. One approach to avoid this problem is to adopt a uniform dataset from a small number of well-calibrated instruments. For example, Konopacky et al. (2016) used data obtained solely from the NIRC2 camera at Keck Observatory to create self-consistent measurements for their orbit fitting. Several other recent studies adopted similar strategies (e.g., Wang et al. 2018b; Gravity Collaboration et al. 2019). However, while this approach may mitigate systematic errors, it also limits the total time baseline and number of astrometric epochs for the orbit fits.

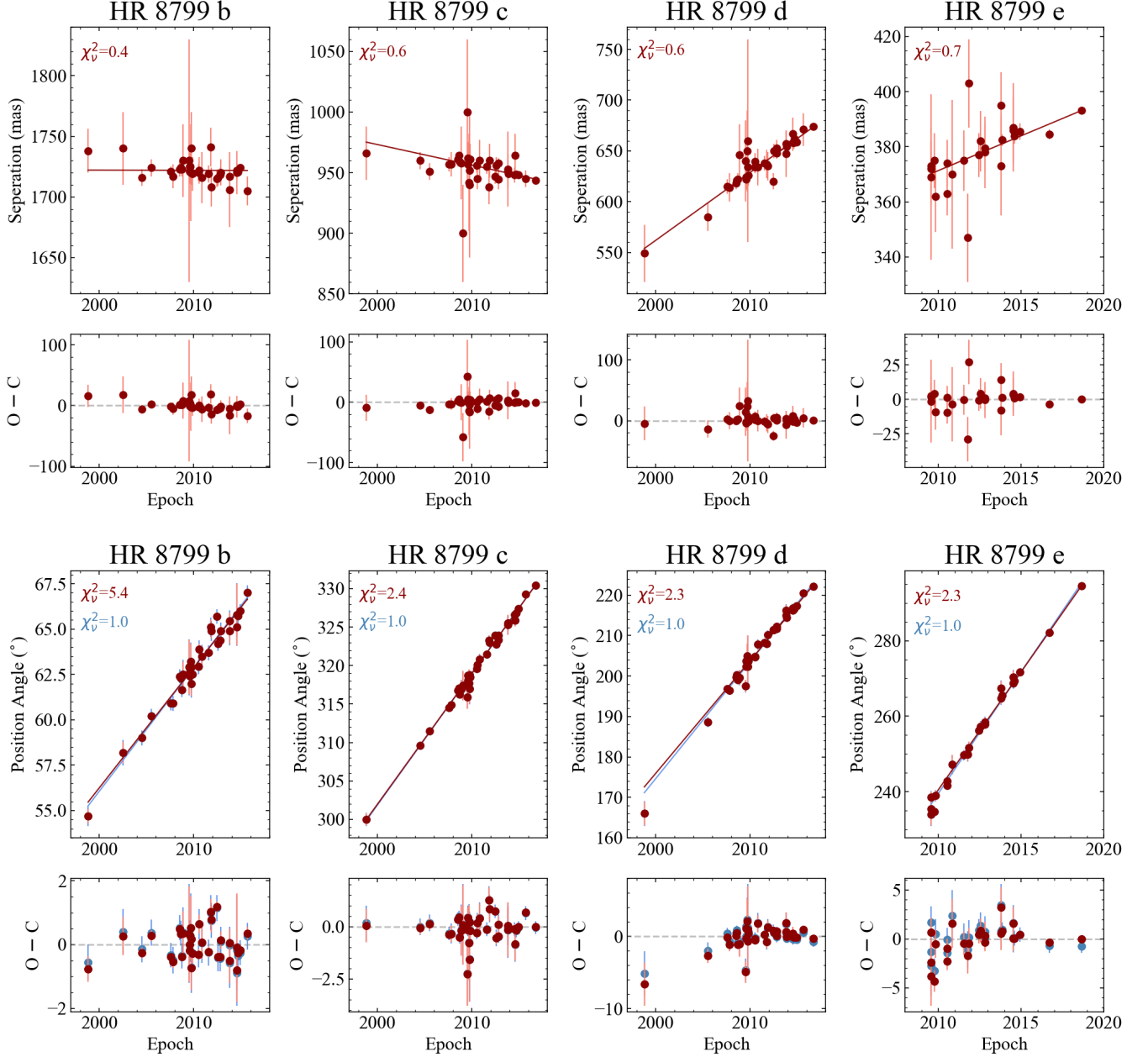


Figure 3. Relative astrometry used in this study as a function of time. The best fitting linear models for $\rho(t)$ and $\theta(t)$ are used to estimate the error inflation and calculate the respective χ^2_ν values. Raw uncertainties are denoted in red. Position angles have an additional systematic uncertainty term added in quadrature (see §3.1), denoted in blue along with corresponding revised linear regression. Uncertainties associated with the separation measurements are left unchanged because the reduced χ^2_ν value of a linear fit to the raw values is < 1.0 for all four planets.

Here we use all available astrometry of the HR 8799 planets as of December 2020 with the goal of maximizing the information content and time baseline of the data. Given that potential systematic uncertainties may affect our dynamical mass measurement, we consider an additional uncertainty term that we refer to as astrometric “jitter” (σ_{jit}) to be added in quadrature to each set of raw astrometric errors following the approach in Bowler et al. (2020). For each planet, we assume a lin-

ear model for both separation (ρ) and position angle (θ) as a function of time because the astrometric time baseline relative to the orbital period is small ($\lesssim 0.16$ for all planets). We adopt a reduced χ^2 value ($\chi^2_\nu \equiv \chi^2/\nu$, where ν is the number of degrees of freedom) as a metric to assess reliability of the quoted uncertainties. The χ^2_ν values for all four planets’ separations as a function of time are < 1.0 (0.37, 0.59, 0.61, and 0.69 for HR 8799 b, c, d, and e, respectively), indicating that the

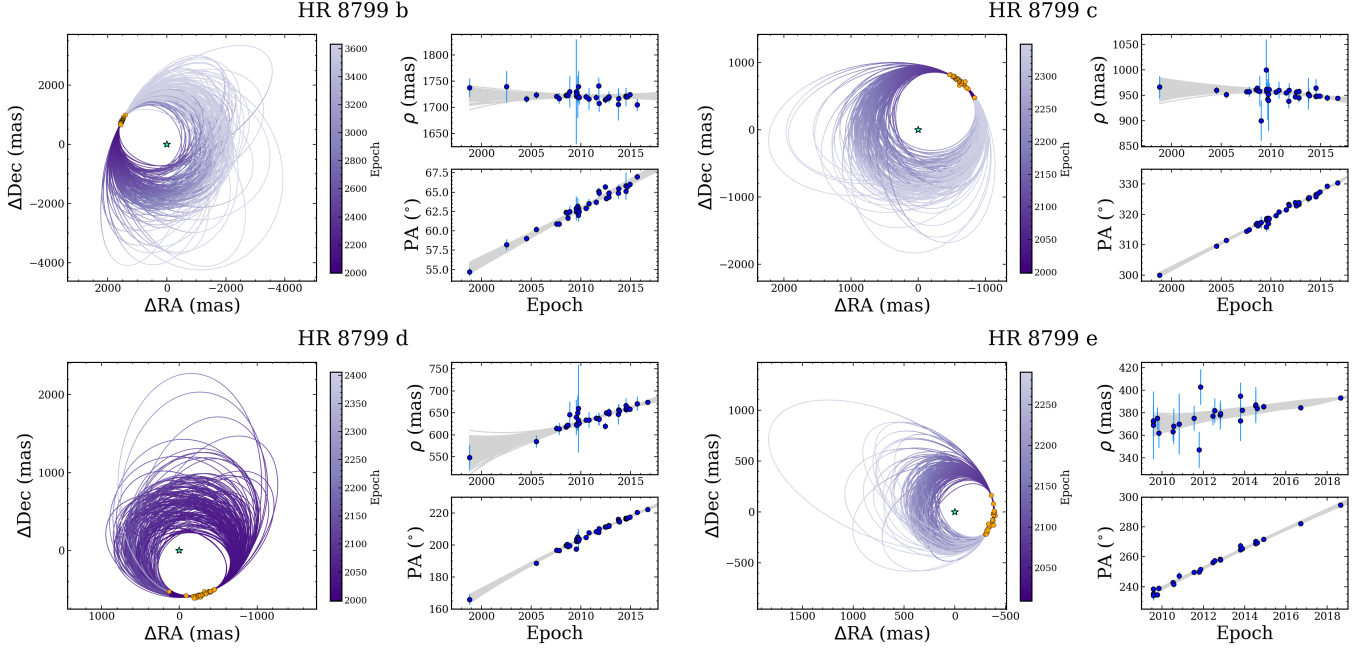


Figure 4. Orbit fits for HR 8799 b, c, d, and e using `orbitize!`. Each panel shows 150 orbits drawn from the converged MCMC chains as described in §3.2 together with the measured astrometry. For each planet, the left panel displays the orbits as they appear on-sky and the right panels compare the same orbits to the astrometry.

raw uncertainties appear to be reasonable. These are left unchanged in this study. However, all four planets' position angles as a function of time have $\chi^2_\nu > 1.0$ (5.4, 2.4, 2.3, and 2.3 for HR 8799 b, c, d, and e, respectively), suggesting that the quoted uncertainties are underestimated or that systematic errors are present. The PA jitter term ($\sigma_{\text{jit,PA}}$) for each planet is found by iteratively increasing a starting value of 0 in steps of 10^{-5} until χ^2_ν reaches unity. This results in $\sigma_{\text{jit,PA}}$ values of 0.37° , 0.26° , 0.62° , and 0.69° for HR 8799 b, c, d and e, respectively. These are added in quadrature to the original uncertainties: $\sigma_{\text{total,PA}}^2 = \sigma_{\text{jit,PA}}^2 + \sigma_{\text{PA}}^2$. The original and adjusted astrometry are displayed in Figure 3.

3.2. Orbit Fitting

We fit Keplerian orbits to the astrometric data of each planet using the `orbitize!` (Blunt et al. 2020) Python package. Here the `ptemcee` (Foreman-Mackey et al. 2013; Vousden et al. 2016) branch is utilized, which samples the posterior distributions of orbital elements with the parallel-tempered affine-invariant ensemble sampler implementation of Markov chain Monte Carlo (MCMC; Goodman & Weare 2010). In the Keplerian model used in `orbitize!`⁴, the following parameters are varied directly when fitting with relative astrometry: a (semi-

major axis), e (eccentricity), i (inclination), ω (argument of periapsis), Ω (position angle of the ascending node), τ (time of last periapsis), π (parallax), and M_{tot} (total mass of the system). We treat each planet independently, corresponding to four separate orbital constraints.

A Gaussian prior of 24.46 mas with a standard deviation of 0.05 mas from *Gaia* EDR3 (Gaia Collaboration et al. 2016, 2021) is used for π . A log-uniform prior distribution is adopted for a (i.e., $P(a) \propto a^{-1}$) with a range of 1 to 150 au. An isotropic inclination distribution is adopted for i such that $P(i) \propto \sin i$ (which spans 0 to π rad). Linearly uniform priors are chosen for the remaining free parameters. Their ranges are: 0 to 1 for e ⁵; 0 to 2π rad for both ω and Ω ; 0 to 1 for τ ; and 0.5 to $4.0 M_\odot$ for M_{tot} . To avoid artificially reducing the precision of the final dynamical mass measurement, we make no further assumptions about the nature of the planets' orbits such as coplanarity, resonances, stability, or orbit crossing events.

Each `ptemcee` ensemble is initialized with 16 temperatures and 1500 walkers per temperature. Each walker samples from the parameter space 1.2×10^5 times and a burn-in length of the first 6.0×10^4 steps is discarded.

⁴ For a more complete description, see Blunt et al. (2020) and <https://orbitize.readthedocs.io>

⁵ Bowler et al. (2020) found that the underlying eccentricity distribution for a sample of 27 imaged substellar companions is approximately uniform, which motivates our use of a linearly uniform eccentricity prior.

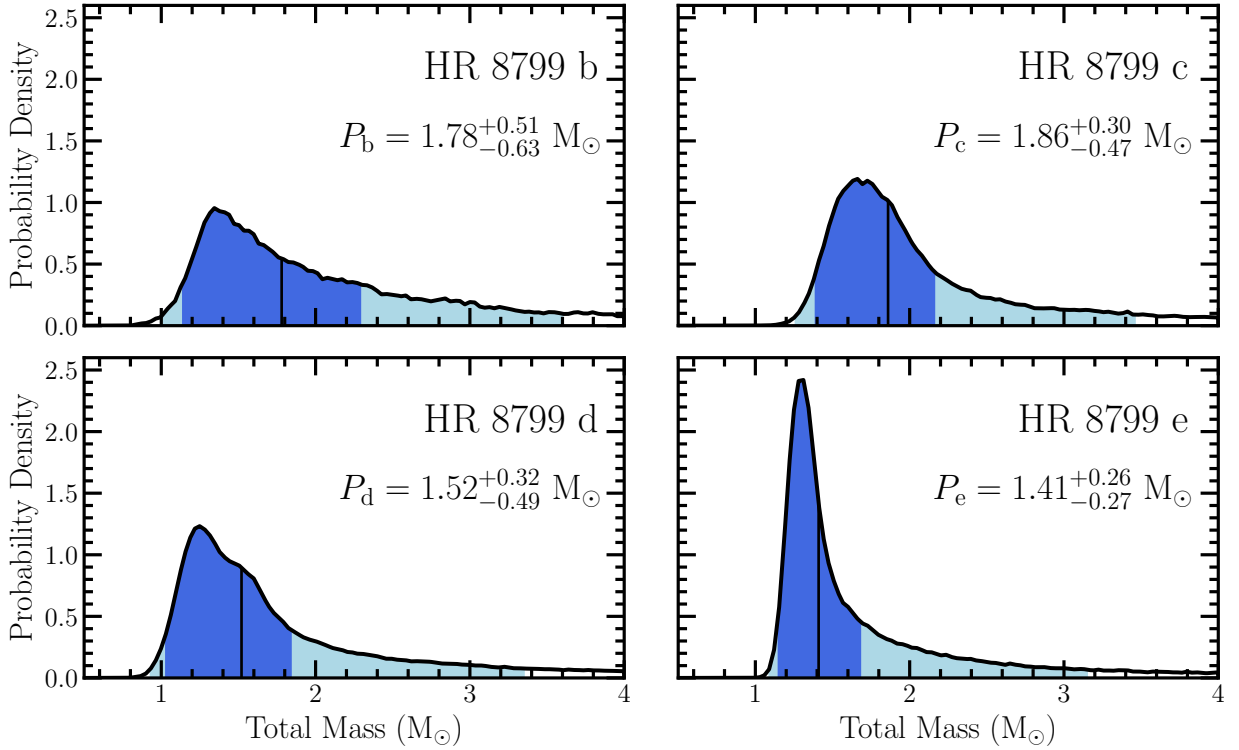


Figure 5. Posterior probability distributions for the total mass of HR 8799 based on orbit fitting for each individual planet as described in §3.2. Dark blue regions represent the 68% HCl and light blue regions represent the 95% HCl. Median values are denoted with a black bar.

To assist their convergence, the walkers are initialized at positions near the most probable values found from conducting preliminary orbit fits. Saving only the samples from the lowest-temperature set of chains and applying a thinning factor of 20 to curtail the effect of correlation results in 4.5×10^6 posterior samples for each orbit fit.

3.3. Bayesian Framework to Constrain the Mass of HR 8799

We employ a Bayesian inference framework to derive the joint probability distribution for the host star mass based on our individual orbit fits for each of the four planets. Bayes’ theorem naturally updates prior information with new data to improve posterior probabilities:

$$P(\theta | D) \propto P(\theta) \times P(D | \theta). \quad (1)$$

Here $P(\theta)$ represents prior knowledge of the parameters θ , $P(D | \theta)$ represents the likelihood function of the data D given the model, and $P(\theta | D)$ represents the posterior probability of the model parameters given the data. For this study of HR 8799, our orbit fits are carried out for a uniform prior distribution in total (stellar) mass, so each of the four total mass posterior distributions from the independent MCMC fits also represent the likelihood

function for the dynamical mass of HR 8799 (to within a constant of proportionality) given the set of astrometry for that planet. This arises by treating the planets as massless “test” particles such that the total mass of the system is assumed to be confined to the host star ($M_p \ll M_*$, or $M_* \approx M_{tot}$). If the HR 8799 planets have masses $\lesssim 10 M_{Jup}$, as expected from evolutionary models (e.g., §5.2), then this approximation is accurate at the $\lesssim 2\%$ level.

We use the following notation to apply Bayes’ Theorem to each of the four independent total mass distributions for planets b, c, d, and e that resulted from orbit fitting:

$$\begin{aligned} P_b &\equiv P(b | M_*), & P_c &\equiv P(c | M_*), \\ P_d &\equiv P(d | M_*), & P_e &\equiv P(e | M_*). \end{aligned} \quad (2)$$

P_i is therefore the likelihood function of the astrometry for planet i conditioned on the stellar (total) mass M_* . The prior probability for M_* , $P(M_*)$, is informed by prior knowledge of the stellar mass (e.g., based on spectral type or evolutionary models). For each iteration of planet b, c, d, and e, the host star mass posterior distribution sequentially becomes the new prior at each stage. For planet b, this is $P(M_* | b) \propto P(M_*) \times P_b$, for

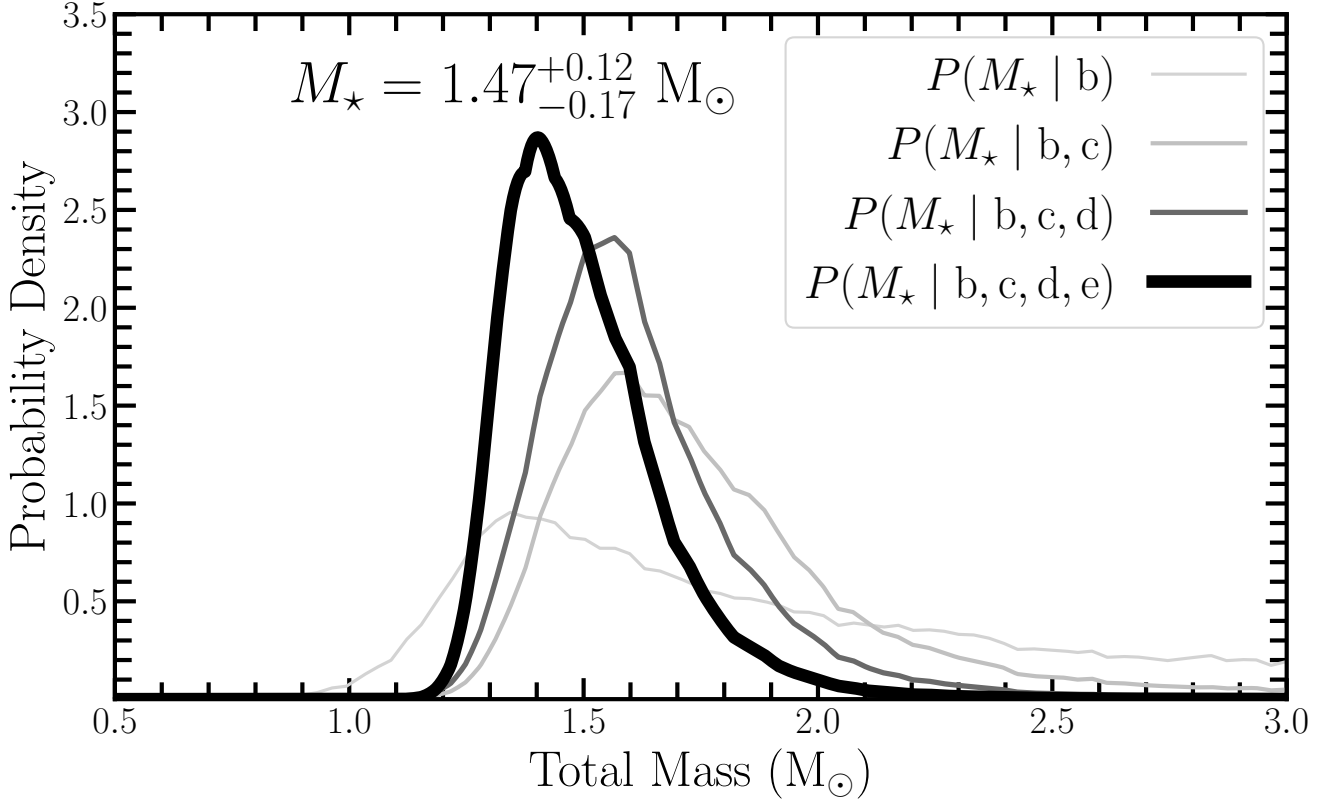


Figure 6. Graphical representation of our Bayesian framework to derive the joint dynamical mass posterior distribution for HR 8799. $P(M_*) | b, c, d, e$ represents the final joint constraint on the dynamical mass of HR 8799 given the astrometry of all four planets and without any assumptions about coplanarity, stability or orbital resonances. This example uses a uniform prior for $P(M_*)$.

planets b and c this is $P(M_*) | b, c) \propto P(M_*) \times P_b \times P_c$, etc. The jointly constrained mass from all four planets is then:

$$P(M_*) | b, c, d, e) \propto P(M_*) \times P_b \times P_c \times P_d \times P_e. \quad (3)$$

This setup allows us to only run the orbit fits once for each planet with a uniform mass prior, but then easily adjust the prior $P(M_*)$ as desired for the joint mass constraint.

4. RESULTS

For each planet, the resulting M_{tot} posterior distributions are linearly interpolated onto a fine grid spanning 0.5–4.0 M_\odot (Figure 5). These are then multiplied together following Equation 3 to arrive at the jointly constrained dynamical mass distribution of HR 8799. Given that the individual total mass constraints are non-Gaussian and right skewed, we summarize the results using the posterior distribution median and highest-density credible interval (HDI) metrics.

For the initializing stellar mass prior $P(M_*)$, we adopt a linearly uniform distribution to let the astrometry

drive the dynamical mass. The final result for this baseline case is shown as Figure 6. The median and 68% HDI of the final joint mass posterior is $1.47^{+0.12}_{-0.17} M_\odot$ ⁶. The 95% and 99.7% HDI span 1.23 – $1.86 M_\odot$ and 1.16 – $2.32 M_\odot$, respectively.

Our choice of a linearly uniform prior may not be especially realistic given that we know HR 8799 is a late-A/early-F star. Our joint stellar mass measurement may be further constrained by using a more informative prior that better captures knowledge of the host star before our experiment takes place while at the same time not being overly restrictive to ensure the astrometry still dominate the posterior. Gray & Kaye (1999) conducted a spectroscopic analysis of HR 8799 and estimated its mass to be $1.47 \pm 0.30 M_\odot$ based on their surface gravity measurement combined with an estimate of the radius. Following the same analysis detailed above but now using this Gaussian prior results in a dynamical mass of $1.46^{+0.11}_{-0.15} M_\odot$ for HR 8799. Here the 95% and

⁶ A log-uniform mass prior proportional to M^{-1} instead of a linearly uniform prior for $P(M_*)$ results in $1.46^{+0.12}_{-0.16} M_\odot$. Both constraints are nearly identical.

99.7% HCI span $1.25\text{--}1.75 M_{\odot}$, and $1.18\text{--}1.97 M_{\odot}$, respectively. The effect of the informed prior is to further reduce the uncertainties on the final joint stellar mass by $\approx 10\%$, which is expected given that this prior is in good agreement with the original dynamical mass (which used a uniform prior).

While not the focus of this study, we summarize results for the orbital parameters from our fits with cornerplots and a table of best-fit values in Appendix A. At the 95% HCI levels, the eccentricities of the planets are constrained to $e \lesssim 0.5$, with the exception of HR 8799 d at $e \lesssim 0.6$. Similarly, at the 68% HCI levels, the eccentricities of planets b, c, and e are constrained to $e \lesssim 0.3$ while HR 8799 d has $e \lesssim 0.4$. This is consistent with previous studies that also found the allowed eccentricities of HR 8799 d to be marginally greater than those of the other three planets (e.g., Pueyo et al. 2015; Wertz et al. 2017). The most probable inclinations for the four planets span $i \approx 25\text{--}35^\circ$, which are similar to each other as well as with that of the extended debris disk ($i \approx 31\text{--}33^\circ$, Wilner et al. 2018; Faramaz et al. 2021). However, the longitude of the ascending node (Ω)⁷ must be accounted for in addition to i to assess coplanarity. For any two orbital planes, these parameters are related to the true mutual inclination ψ by the geometric relation $\psi = \arccos(\cos i_1 \cos i_2 + \sin i_1 \sin i_2 \cos(\Omega_1 - \Omega_2))$. We place a 95% confidence upper limit of $\psi < 55 - 75^\circ$ for all permutations of the HR 8799 planet orbital planes. Orbital parameters in this study are generally consistent with results from prior published orbit fits, although our posteriors tend to be larger. This is an expected consequence of our methodology: we solved for the total system mass using agnostic priors, made no constraining assumptions on allowed orbits based on stability, and inflated the astrometric uncertainties to account for potential systematic errors.

4.1. Low-Eccentricity Scenario

The posteriors in Figure 8 show that there is strong covariance between planet eccentricities and total system mass; higher planet eccentricities imply a substantially larger total mass. To assess how the cumulative dynamical mass might change if near-circular orbits are considered, we reconduct the analysis in an identical manner but we now limit the possible orbit solutions for each planet to $e \leq 0.1$. Although low eccentricities

⁷ Orbit fitting with only relative astrometry suffers from a 180° degeneracy for both Ω and ω . In this work, we wrap all posteriors of Ω and ω from $[0, 360]^\circ$ to $[0, 180]^\circ$. While beyond the scope of this study, radial velocities of the planets can be used to break the $\omega - \Omega$ degeneracy. See, e.g., Wang et al. (2018a); Ruffio et al. (2019, 2021) and Wang et al. (2021).

on their own are not necessarily indicative of orbital stability (e.g., Fabrycky & Murray-Clay 2010), this exercise gives some insight into how the stellar mass constraint depends on eccentricity and what we might expect if long-term orbital stability is taken into account⁸. The joint dynamical mass in this scenario of near-circular orbits is $1.43_{-0.07}^{+0.06} M_{\odot}$, with 95% and 99.7% HCI intervals spanning $1.31\text{--}1.57 M_{\odot}$ and $1.28\text{--}1.65 M_{\odot}$, respectively. The smaller uncertainties are expected given the strong correlation between eccentricity and total mass in our baseline orbit fit. Using the informed Gaussian mass prior of $1.47 \pm 0.30 M_{\odot}$ does not significantly influence the joint stellar mass constraint ($M_{\star} = 1.43_{-0.07}^{+0.06} M_{\odot}$ in this scenario). The orbit fitting results for this low eccentricity scenario are presented in Appendix B. We conclude that a restricted eccentricity significantly impacts the dynamical mass by reducing the overall uncertainty by a factor of ≈ 2 . For this study, however, we adopt the unrestricted solution in which eccentricity is allowed to vary from 0 to 1 to avoid assumptions about mutual planet interactions, which are not yet robustly validated by the astrometry.

5. DISCUSSION

We fit orbits to all the available astrometry of the HR 8799 planets with minimal dynamical assumptions, then combined the independent total mass constraints into a joint dynamical mass measurement. Table 1 from Baines et al. (2012) compiles many of the existing mass estimates of HR 8799, which have been determined with a variety of methods and generally span the range of $\sim 1.2\text{--}1.8 M_{\odot}$. Our dynamical mass measurement is consistent with all these prior estimates at its 95% HCI level, including the estimates of $1.513_{-0.024}^{+0.023} M_{\odot}$ and $1.516_{-0.024}^{+0.038} M_{\odot}$ derived by Baines et al. (2012) from their measured stellar parameters together with Yonsei-Yale (Yi et al. 2001) evolutionary models. Our dynamical mass measurement thus serves as a reassuring validation of the $\approx 1.5 M_{\odot}$ stellar mass commonly adopted in previous studies of the HR 8799 system.

Wang et al. (2018b) used a self-consistent astrometric dataset from NIRC2 and GPI (55 epochs in total) to simultaneously measure the companion orbital parameters and total mass of HR 8799 in an MCMC framework. In their “unconstrained” fits, they found a total mass of $1.48_{-0.04}^{+0.05} M_{\odot}$ which, under the approximation $M_{\star} \approx M_{tot}$, can be considered another dynamical mass

⁸ For robust explorations and discussion of the dynamical stability of the HR 8799 planets, we defer to recent studies by, e.g., Wang et al. (2018b), Goździewski & Migaszewski (2018, 2020), and Veras & Hinkley (2021).

measurement of HR 8799 to compare with ours. The larger uncertainties in this study are likely influenced by our adoption of a linearly uniform total mass prior compared to their adoption of a well-informed Gaussian prior of $1.52 \pm 0.15 M_{\odot}$. Furthermore, by using a dataset only from NIRC2 and GPI without the inflated astrometric uncertainty that we accounted for, their astrometric measurement uncertainties were overall smaller compared to the astrometry used in this study. However, despite some differences in procedure and data used, both results agree well. The dynamical mass presented in this work should be considered a conservative, model-independent measurement that prioritized astrometric baseline over per-epoch precision and instrument uniformity.

5.1. Age of HR 8799

Several stellar parameters of HR 8799 (radius, luminosity, and effective temperature) were directly constrained by [Baines et al. \(2012\)](#) using a Center for High Angular Resolution Astronomy (CHARA) Array stellar angular diameter measurement together with photometry and the parallax from Hipparcos. They found a radius of $R_{\star} = 1.44 \pm 0.06 R_{\odot}$, a bolometric luminosity of $L_{\star} = 5.05 \pm 0.29 L_{\odot}$, and an effective temperature of $T_{\text{eff}} = 7193 \pm 87$ K; these are based on a bolometric flux of $F_{\text{bol}} = (1.043 \pm 0.012) \times 10^{-7}$ erg s $^{-1}$ cm $^{-2}$, an angular diameter (accounting for limb darkening) of $\theta_{\text{LD}} = 0.342 \pm 0.008$ mas, and a distance of $D_{\star} = 39.4 \pm 1.0$ pc ([van Leeuwen 2007](#)). [Faramaz et al. \(2021\)](#) updated and improved the statistical uncertainties for several of these values. They found $L_{\star} = 5.441 \pm 0.066 L_{\odot}$ using the bolometric flux from [Baines et al. \(2012\)](#) together with a distance of 40.851 ± 0.076 pc from *Gaia* EDR3 ([Gaia Collaboration et al. 2021; Lindegren et al. 2021](#)). They also updated the radius to $R_{\star} = 1.502 \pm 0.035 R_{\odot}$ when using their *Gaia* EDR3 distance together with the stellar angular diameter from [Baines et al. \(2012\)](#).

The measured mass, luminosity, radius, and effective temperature of HR 8799 (Table 2) can be used to constrain its bulk metallicity and age using stellar evolutionary models. We downloaded a custom grid of MESA Isochrones & Stellar Tracks (MIST) evolutionary models ([Paxton et al. 2011, 2013, 2015, 2018; Dotter 2016; Choi et al. 2016](#)) spanning $M_{\star} = 0.5 \text{--} 4.0 M_{\odot}$ ($\Delta M_{\star} = 0.01 M_{\odot}$) for four metallicities⁹: $[\text{Fe}/\text{H}] = -0.5, -0.25, 0.0, \text{ and } +0.25$ dex. A surface angular velocity at 40% of the critical value is adopted following [Choi et al. \(2016\)](#); however, the effect of rotation and surface mass loss is minimal in this mass regime. Intermediate-mass stars

Table 2. Measured Fundamental Stellar Parameters of HR 8799

Parameter	Value	References
M_{\star} (M_{\odot})	$1.47^{+0.12}_{-0.17}^{\text{a}}$	1
R_{\star} (R_{\odot})	1.502 ± 0.035	2,3
L_{\star} (L_{\odot})	5.441 ± 0.066	2,3
T_{eff} (K)	$7193 \pm 87^{\text{b}}$	3

References—(1) This work (assumes a uniform stellar mass prior); (2) [Faramaz et al. \(2021\)](#); (3) [Baines et al. \(2012\)](#)

^aUsing an informed Gaussian stellar mass prior results in $1.46^{+0.11}_{-0.15} M_{\odot}$.

^b[Boyajian et al. \(2013\)](#) find a consistent value of $T_{\text{eff}} = 7163 \pm 84$ K using the stellar angular diameter from [Baines et al. \(2012\)](#) together with their own calculation of the stellar bolometric flux.

like HR 8799 follow a meandering trajectory through the HR diagram as they quickly reach the main sequence and then evolve off it. In doing so their luminosity and effective temperature will repeatedly rise and fall. As a result, a given luminosity and temperature can correspond to two or more degenerate ages during the pre- and post-main sequence evolutionary phases. The additional mass and radius measurements help by limiting the ages consistent with all of these constrained parameters.

We begin our assessment of the bulk metallicity and age by randomly drawing a stellar mass rounded to the nearest $0.01 M_{\odot}$ with a probability proportional to the dynamical mass posterior distribution of HR 8799 found in §4. We also draw a luminosity from a normal distribution with a mean of $5.441 L_{\odot}$ and a standard deviation of $0.066 L_{\odot}$. The iso-mass track will either be inconsistent with the given luminosity throughout the entire evolution of that star, or it will intersect the given luminosity at least once. If the former occurs, that trial is ignored and another mass is drawn; for the latter, ages are interpolated across the grid sampling at the luminosity crossing point. If the corresponding model radius and temperature at that point are within 3σ of the measured values of $1.502 \pm 0.035 R_{\odot}$ and 7193 ± 87 K, respectively, then the ages are retained. This process of drawing a mass and luminosity and saving ages consistent with the models is repeated 10^4 times to build up a distribution of ages consistent with the measured values. Results for the linearly uniform mass prior are shown in Figure 7.

⁹ Here $[\text{Z}/\text{H}] = [\text{Fe}/\text{H}]$, the solar-scaled bulk metallicity.

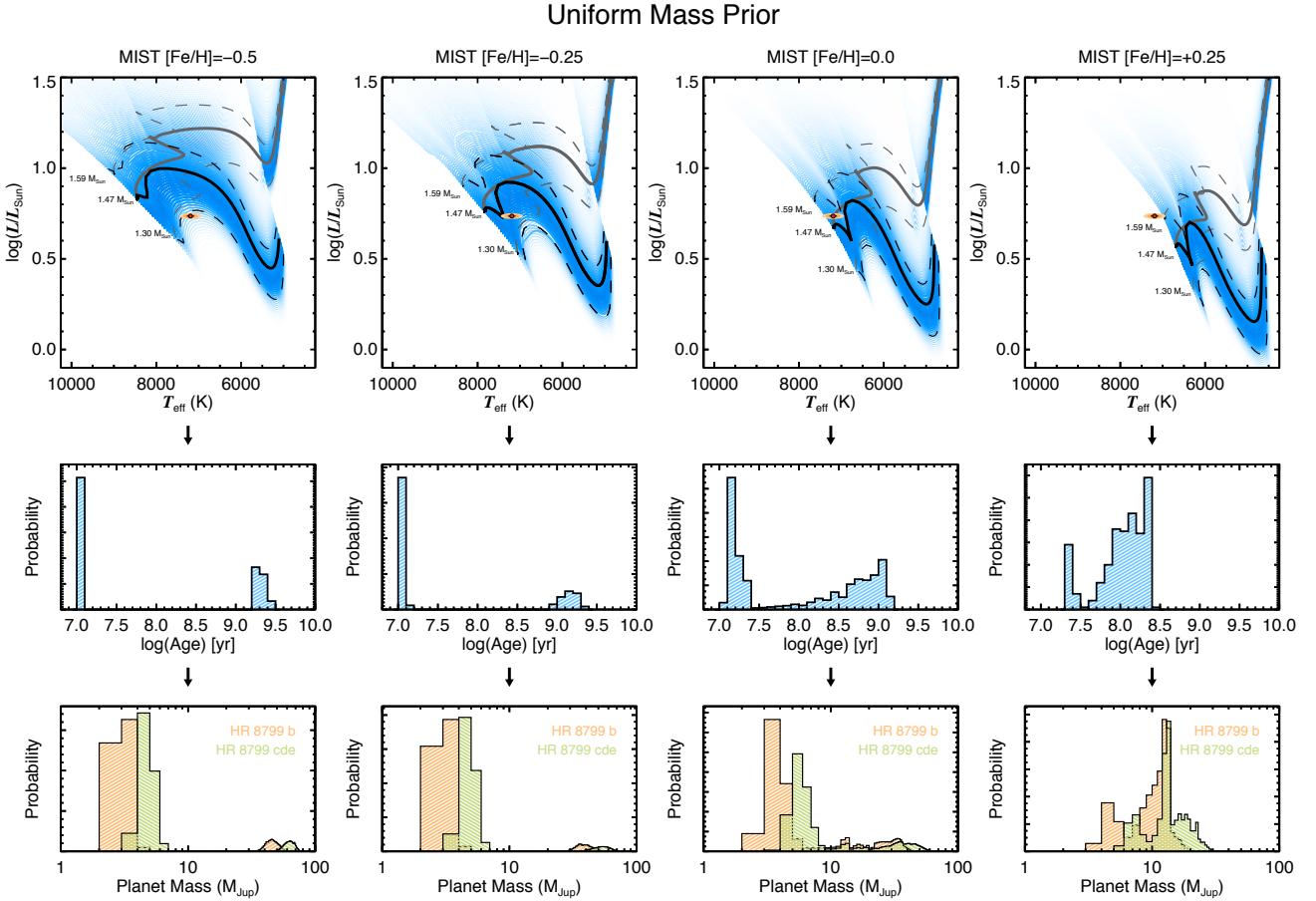


Figure 7. *Top Row:* MESA iso-mass tracks used to construct the age distributions of HR 8799. The thickness and color of each track is proportional to the probability density of the joint dynamical mass posterior distribution of HR 8799 at that model value. The solid black and gray line denotes the evolutionary track corresponding to the median value of our dynamical mass posterior. It is shown in black for the pre-main sequence phase of evolution and then becomes gray for the post-main sequence phase. Similarly, the dashed black and gray lines correspond to the 68% HCl. Each column of panels corresponds to a different metallicity from $[\text{Fe}/\text{H}] = -0.5$ to $+0.25$ dex. The orange ellipse represents the measurement and 1-, 2-, and 3- σ uncertainties of L_* and T_{eff} for HR 8799. *Middle Row:* The inferred age distributions of HR 8799 following the method described in §5.1. *Bottom Row:* Corresponding hot-start masses for the planets derived directly from the age distribution and planet luminosities.

Our use of four different $[\text{Fe}/\text{H}]$ values enables a qualitative constraint of the stellar bulk metallicity: the stellar parameters are most consistent with $[\text{Fe}/\text{H}] \sim -0.25$ –0.00 dex but only marginally consistent with $[\text{Fe}/\text{H}] = -0.5$ and $+0.25$ dex. The λ Bootis nature of HR 8799 has made previous attempts to characterize the bulk metallicity difficult because the surface abundances may not be an accurate tracer of the internal composition (e.g., Moya et al. 2010b; Murphy et al. 2021). In spite of the coarse sampling in the metallicities as well as potential systematic uncertainties in the MESA grids themselves, these qualitative constraints support a picture in which HR 8799 may have a solar-like or slightly sub-solar bulk composition.

There are two general solutions for the age of HR 8799 that correspond to an ambiguity related to whether it is moving toward or evolving from the zero age main sequence. For the $[\text{Fe}/\text{H}] = 0.00$ dex grids, these correspond to ages of $\sim 10^{7-7.4}$ yr and $\sim 10^{8-9.1}$ yr. Fabrycky & Murray-Clay (2010) found that the outer three HR 8799 planets must be $\lesssim 20 M_{\text{Jup}}$ to remain stable on timescales of tens of Myr. Motivated by this dynamical stability requirement, we ignore the older age scenario because this results in implausibly high planet masses up to the hydrogen-burning limit. For each metallicity grid, we discard ages corresponding to a planet mass cutoff of $> 20 M_{\text{Jup}}$ using hot-start evolutionary models (see §5.2).

Excluding the $[\text{Fe}/\text{H}] = +0.25$ dex grids, which are least consistent with the measured properties of HR 8799, an age of 10–23 Myr best agrees with our dynamical mass. This is younger than the age of 38–48 Myr (Bell et al. 2015) that is associated with HR 8799 if it is a member of the Columba moving group. This is also somewhat younger than the hot-start cooling age of 42^{+24}_{-16} Myr for HR 8799 e recently derived by Brandt et al. (2021b), although at twice their quoted uncertainties, both ages are consistent. Baines et al. (2012) use Yonsei-Yale grids fixed at solar metallicity to derive an age consistent with either ~ 33 Myr or ~ 90 Myr. Regardless of kinematic association with a young moving group, these model-based constraints all support the picture that the HR 8799 system is < 100 Myr and probably younger than 50 Myr.

To assess the impact of mass priors and restricted eccentricities on the results, we repeat this exercise for the other three scenarios considered in §4: the dynamical mass with the informed Gaussian prior, and the two low-eccentricity cases. Summary statistics for the resulting trimmed distributions are tabulated in Table 3. Figures showing the ages and corresponding hot-start masses using our other dynamical masses under different assumptions for the mass prior and range of eccentricities can be found in Appendix C. The values of the ages and hot-start masses do not significantly change depending on which dynamical mass is used, and the constraints of $[\text{Fe}/\text{H}]$ also remain consistent.

5.2. Hot-Start Mass Constraints of the Planets

In light of these revised age estimates, we use hot-start evolutionary models from Burrows et al. (1997) to infer the masses of the imaged companions using their bolometric luminosities (Figure 7). Here we assume the age of the star to be the age of the planets. For planet b, we adopt a bolometric luminosity of $\log(L_{\text{bol}}/\text{L}_\odot) = -5.1 \pm 0.1$ dex, and for planets c and d we adopt $\log(L_{\text{bol}}/\text{L}_\odot) = -4.7 \pm 0.1$ dex (Marois et al. 2008; Rajan et al. 2015). The spectrum and near-infrared contrast of planet e is similar to that of planets c and d (e.g., Marois et al. 2010; Greenbaum et al. 2018), thus we adopt the same value of $\log(L_{\text{bol}}/\text{L}_\odot) = -4.7 \pm 0.1$ dex for this inner planet.

Excluding the $[\text{Fe}/\text{H}] = +0.25$ dex grids and the discarded solutions corresponding to old ($\sim \text{Gyr}$) ages, the resulting mass estimates are $2.7\text{--}4.9 \text{ M}_{\text{Jup}}$ for HR 8799 b and $4.1\text{--}7.0 \text{ M}_{\text{Jup}}$ for HR 8799 c, d, and e (Table 3). These masses are within the giant planet regime assuming a boundary of $\approx 13 \text{ M}_{\text{Jup}}$ and are lower than, but still broadly consistent with, many of the previous estimates in the literature. For example, Marois et al.

Table 3. HR 8799 Age and Planet Masses from MIST Models^a

Model		Age	Mass
$[\text{Fe}/\text{H}]$	Planet	(Myr)	(M_{Jup})
Uniform Mass Prior			
+0.25	b	120^{+130}_{-40}	12^{+2}_{-3}
0.0	b	17^{+6}_{-5}	$4.0^{+0.9}_{-1.3}$
-0.25	b	$11.3^{+1.2}_{-1.2}$	$3.1^{+0.4}_{-0.4}$
-0.50	b	$11.3^{+1}_{-1.2}$	$3.1^{+0.4}_{-0.4}$
+0.25	c/d/e	120^{+130}_{-40}	$13.2^{+5.3}_{-1.5}$
0.0	c/d/e	17^{+6}_{-5}	$6.0^{+1}_{-1.4}$
-0.25	c/d/e	$11.3^{+1.2}_{-1.2}$	$4.8^{+0.5}_{-0.7}$
-0.50	c/d/e	$11.3^{+1}_{-1.2}$	$4.8^{+0.5}_{-0.7}$
Normal Mass Prior			
+0.25	b	140^{+110}_{-50}	$12.1^{+1.5}_{-3.5}$
0.0	b	17^{+6}_{-5}	$4.0^{+0.9}_{-1.2}$
-0.25	b	$11.3^{+1.2}_{-1.2}$	$3.1^{+0.4}_{-0.4}$
-0.50	b	$11.2^{+0.98}_{-1.2}$	$3.0^{+0.4}_{-0.4}$
+0.25	c/d/e	140^{+110}_{-50}	$13.4^{+6.3}_{-0.84}$
0.0	c/d/e	17^{+6}_{-5}	$6.0^{+1}_{-1.4}$
-0.25	c/d/e	$11.3^{+1.2}_{-1.2}$	$4.8^{+0.5}_{-0.7}$
-0.50	c/d/e	$11.2^{+0.98}_{-1.2}$	$4.8^{+0.5}_{-0.7}$
Uniform Mass Prior, Low Eccentricities			
+0.25	b	140^{+100}_{-40}	$12.3^{+1.3}_{-2.4}$
0.0	b	19^{+36}_{-9}	$4.3^{+3.4}_{-1.9}$
-0.25	b	$11.3^{+1.2}_{-1.2}$	$3.1^{+0.4}_{-0.4}$
-0.50	b	$11^{+1}_{-1.1}$	$3.1^{+0.4}_{-0.4}$
+0.25	c/d/e	140^{+100}_{-40}	$13.5^{+4.8}_{-1.1}$
0.0	c/d/e	19^{+36}_{-9}	$6.2^{+1.1}_{-1.6}$
-0.25	c/d/e	$11.3^{+1.2}_{-1.2}$	$4.8^{+0.5}_{-0.7}$
-0.50	c/d/e	$11.2^{+1}_{-1.1}$	$4.8^{+0.5}_{-0.7}$
Normal Mass Prior, Low Eccentricities			
+0.25	b	120^{+150}_{-57}	12^{+2}_{-5}
0.0	b	19^{+4}_{-7}	$4.3^{+2.9}_{-1.9}$
-0.25	b	$11.3^{+1.2}_{-1.2}$	$3.1^{+0.4}_{-0.4}$
-0.50	b	$11.2^{+1.0}_{-1.2}$	$3.0^{+0.4}_{-0.4}$
+0.25	c/d/e	120^{+150}_{-57}	$13.1^{+1.9}_{-6.7}$
0.0	c/d/e	19^{+4}_{-7}	$6.2^{+1.1}_{-1.5}$
-0.25	c/d/e	$11.3^{+1.2}_{-1.2}$	$4.8^{+0.5}_{-0.7}$
-0.50	c/d/e	$11.2^{+1.0}_{-1.2}$	$4.8^{+0.5}_{-0.7}$

^a Assumes dynamical stability in which planet masses $> 20 \text{ M}_{\text{Jup}}$ are excluded.

(2008) and Marois et al. (2010) report hot-start masses of 5–7 M_{Jup} for planet b and 7–10 M_{Jup} for planets c, d, and e for ages of 30 Myr and 60 Myr. Wilner et al. (2018) estimated a dynamical mass of HR 8799 b to be $5.8^{+7.9}_{-3.1} M_{Jup}$ if it is responsible for clearing mass in its chaotic zone out to the inner edge of the debris disk. Within their subset of dynamically stable orbital solutions, Wang et al. (2018b) find hot-start masses of $5.8 \pm 0.5 M_{Jup}$ for planet b and $7.2^{+0.6}_{-0.7} M_{Jup}$ for planets c, d, and e for an age of 42 ± 5 Myr. Brandt et al. (2021b) recently presented a dynamical mass of $9.6^{+1.9}_{-1.8} M_{Jup}$ for HR 8799 e by using a *Gaia* EDR3 host star proper motion anomaly together with results from Wang et al. (2018b) for orbital solutions and planet mass ratios. This is somewhat higher than the values we found and could be caused by an underestimated age, compositional difference between the star and planet, higher planet luminosity, or systematic errors in the models themselves. Altogether, the mass estimates presented in this work imply a minimum-mass extrasolar nebula of $M \geq 15$ – $26 M_{Jup}$ for HR 8799.

6. CONCLUSION

We have measured the model-independent dynamical mass of HR 8799 in a Bayesian framework using all available astrometry of its four planets and treating them as massless independent particles. The joint dynamical mass of HR 8799 is $1.47^{+0.12}_{-0.17} M_{\odot}$ assuming a uniform prior, validating regularly used values of $\approx 1.5 M_{\odot}$ in previous studies. The modest but realistic uncertainties improve to $1.46^{+0.11}_{-0.15} M_{\odot}$ when an informative prior based on the stellar spectroscopy is used. When only near-circular orbits of $e < 0.1$ are allowed, the joint dynamical mass measurement becomes $1.43^{+0.06}_{-0.07} M_{\odot}$.

We used our stellar mass constraints together with other previously measured parameters of the host star to investigate the age and bulk metallicity of HR 8799. The age constraint from MESA models is 10–23 Myr after excluding ages corresponding to hot-start masses of $\geq 20 M_{Jup}$. This supports an intermediate age for this system independent of kinematic membership status to young moving groups. We also find that the favored bulk metallicity is $[Fe/H] \sim -0.25$ – 0.00 dex.

Finally, using these inferred ages, we derived hot start masses of 2.7 – $4.9 M_{Jup}$ for HR 8799 b and 4.1 – $7.0 M_{Jup}$ for HR 8799 c, d, and e. These are somewhat lower than typical estimates, as expected from the younger inferred age. Continued astrometric monitoring of this system will enable future studies to progressively reduce the uncertainty in the orbital elements of the planets and the mass of HR 8799. However, eventually the assumption that $M_{\star} \approx M_{tot}$ will break down as the total mass

precision becomes comparable to the planet masses. At that point, a more complete dynamical modeling that includes mutual planet interactions will be needed to properly account for the total system mass interior to each orbit (e.g., Lacour et al. 2021).

Acknowledgments. We thank the anonymous referee for constructive suggestions as well as Henry Ngo and Sarah Blunt for their consulting with the `orbitize!` package.

A.G.S acknowledges support from the Texas Astronomy Undergraduate Research experience for Underrepresented Students (TAURUS) Scholars program. TAURUS graciously acknowledges funding from the National Science Foundation (NSF), National Aeronautics and Space Administration (NASA), the Cox Board of Visitors for the University of Texas’ Department of Astronomy and McDonald Observatory, and many generous donors who gave to the TAURUS HornRaiser campaign. TAURUS is also grateful for the countless time commitments of students, staff, and faculty at UT to build a healthier, happier, and more representative astronomy community. This material is based upon work supported by the National Science Foundation Graduate Research Fellowship Program under Grant No. 1842402. B.P.B. acknowledges support from the National Science Foundation grant AST-1909209 and NASA Exoplanet Research Program grant 20-XRP20-2-0119.

This work received computational support from UTSA’s HPC cluster SHAMU, operated by the Office of Information Technology. A.G.S. thanks Eric Schlegel for the sponsorship that enabled the use of this resource.

Some of the data presented herein were obtained at the W. M. Keck Observatory, which is operated as a scientific partnership among the California Institute of Technology, the University of California and the National Aeronautics and Space Administration. The Observatory was made possible by the generous financial support of the W. M. Keck Foundation. The authors wish to recognize and acknowledge the very significant cultural role and reverence that the summit of Maunakea has always had within the indigenous Hawaiian community. We are most fortunate to have the opportunity to conduct observations from this mountain.

This work has made use of data from the European Space Agency (ESA) mission *Gaia* (<https://www.cosmos.esa.int/gaia>), processed by the *Gaia* Data Processing and Analysis Consortium (DPAC, <https://www.cosmos.esa.int/web/gaia/dpac/consortium>). Funding for the DPAC has been provided by national institu-

tions, in particular the institutions participating in the *Gaia* Multilateral Agreement.

This research has made use of NASA’s Astrophysics Data System Bibliographic Services.

Software: `orbitize!` (Blunt et al. 2020), `ptemcee` (Foreman-Mackey et al. 2013; Vousden et al. 2016), `matplotlib` (Hunter 2007), `numpy` (van der Walt et al. 2011; Harris et al. 2020), `astropy` (Astropy Collaboration et al. 2013, 2018)

Facility: Keck:II (NIRC2)

APPENDIX

A. ORBIT FITTING RESULTS

Corner plots showing the two-dimensional joint posterior distributions for each combination of parameters from our MCMC orbit fit of HR 8799 b, c, d, and e are shown in Figure 8. These results are for a uniform prior on stellar mass and summarized in Table 4. The marginalized posterior distributions for the orbital parameters are displayed along the diagonal, and M_{tot} is highlighted in the upper right. The contours of the 2-D histograms are 68.3%, 95.4%, and 99.7% density levels.

B. LOW-ECCENTRICITY ORBIT FITTING RESULTS

The results of our MCMC orbit fits for the low-eccentricity scenario are summarized in Figure 9 and Table 5. We also display a sample of the sky-projected orbits drawn from the MCMC chains in Figure 10.

C. MESA AGES AND HOT-START PLANET MASSES

This Appendix includes a summary of results from stellar and substellar evolutionary models following our procedure described in §5.1 but using the other three dynamical masses from §4. Figure 11 shows results using the dynamical mass with the informed Gaussian prior. Results with the low-eccentricity assumption using the dynamical mass with a uniform prior and with the informed Gaussian prior are displayed in Figures 12 and 13, respectively.

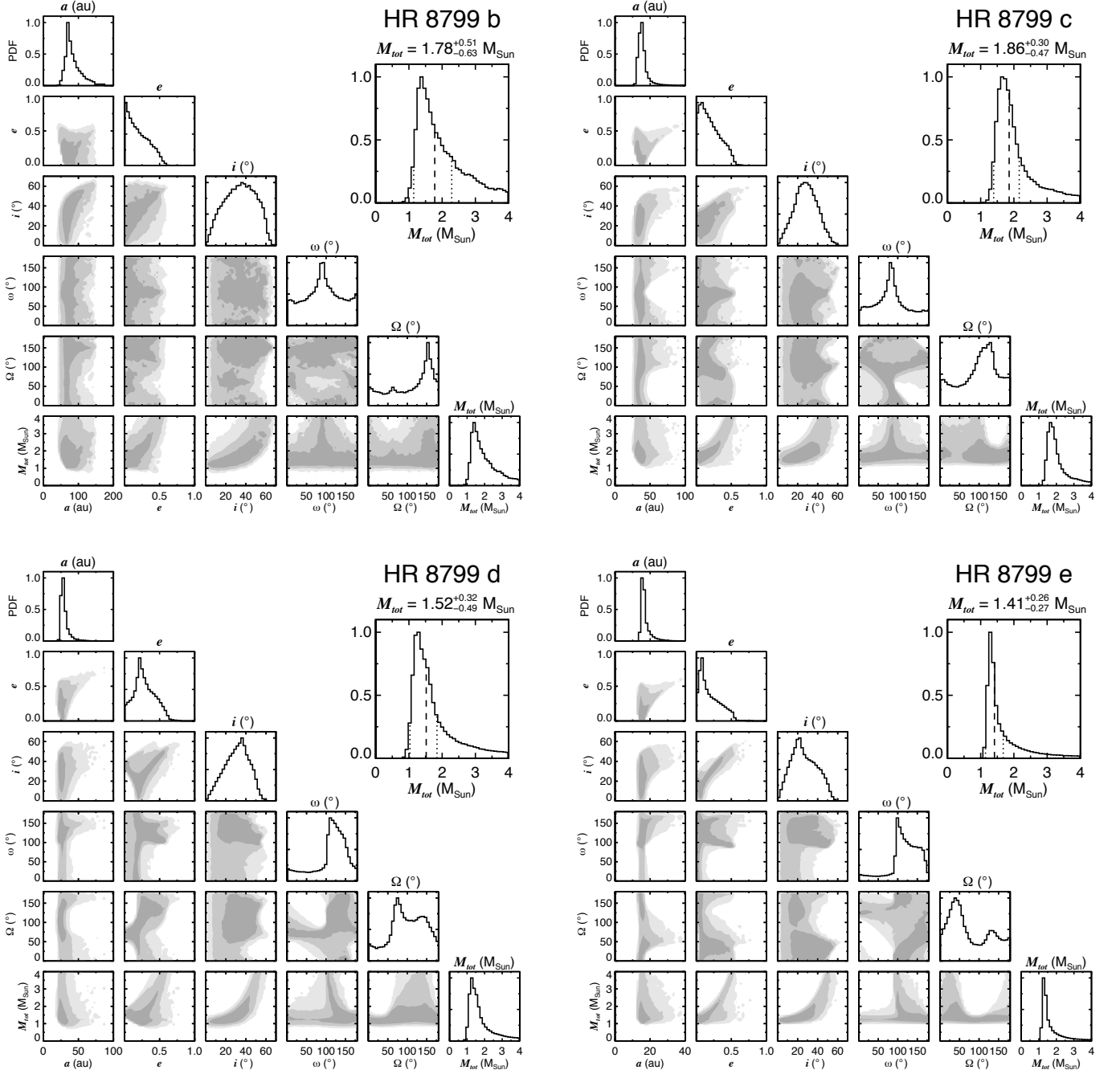


Figure 8. Summary of the MCMC orbit-fitting results for a uniform prior on stellar host mass.

Table 4. HR 8799 Orbit Fit Results

Parameter	Median	MAP ^a	68.3% CI	95.4% CI
HR 8799 b				
a (AU)	77.9	70.5	(59.6, 94.4)	(50.1, 132)
e	0.17	0.015	(0.0, 0.27)	(0.0, 0.48)
i ($^{\circ}$)	35	37	(20, 53)	(7, 60)
ω ($^{\circ}$)	91	91	(47, 155)	(10, 180)
Ω ($^{\circ}$)	128	154	(84, 180)	(9.6, 180)
M_{tot} (M_{\odot})	1.78	1.35	(1.14, 2.29)	(1.0, 3.60)
HR 8799 c				
a (AU)	38.2	39.5	(32.3, 41.4)	(29.2, 55.3)
e	0.18	0.06	(0.0, 0.27)	(0.0, 0.48)
i ($^{\circ}$)	28	25	(17, 40)	(6, 51)
ω ($^{\circ}$)	83	84	(22, 116)	(2, 169)
Ω ($^{\circ}$)	108	127	(78, 173)	(10, 180)
M_{tot} (M_{\odot})	1.86	1.67	(1.39, 2.16)	(1.26, 3.46)
HR 8799 d				
a (AU)	28.5	26.5	(24.4, 31.1)	(22.8, 42.9)
e	0.27	0.21	(0.13, 0.44)	(0.0, 0.56)
i ($^{\circ}$)	32	36	(20, 45)	(7, 52)
ω ($^{\circ}$)	120	111	(102, 161)	(17, 180)
Ω ($^{\circ}$)	100	74	(63, 151)	(18, 180)
M_{tot} (M_{\odot})	1.52	1.25	(1.03, 1.84)	(0.93, 3.35)
HR 8799 e				
a (AU)	16.2	15.5	(14.5, 17.3)	(14.0, 23.9)
e	0.16	0.06	(0.0, 0.26)	(0.0, 0.49)
i ($^{\circ}$)	25	22	(12, 39)	(5, 51)
ω ($^{\circ}$)	119	97	(94, 154)	(30, 180)
Ω ($^{\circ}$)	59	39	(0.0, 105)	(0.074, 169)
M_{tot} (M_{\odot})	1.41	1.29	(1.15, 1.68)	(1.09, 3.15)

^aMaximum a posteriori probability.

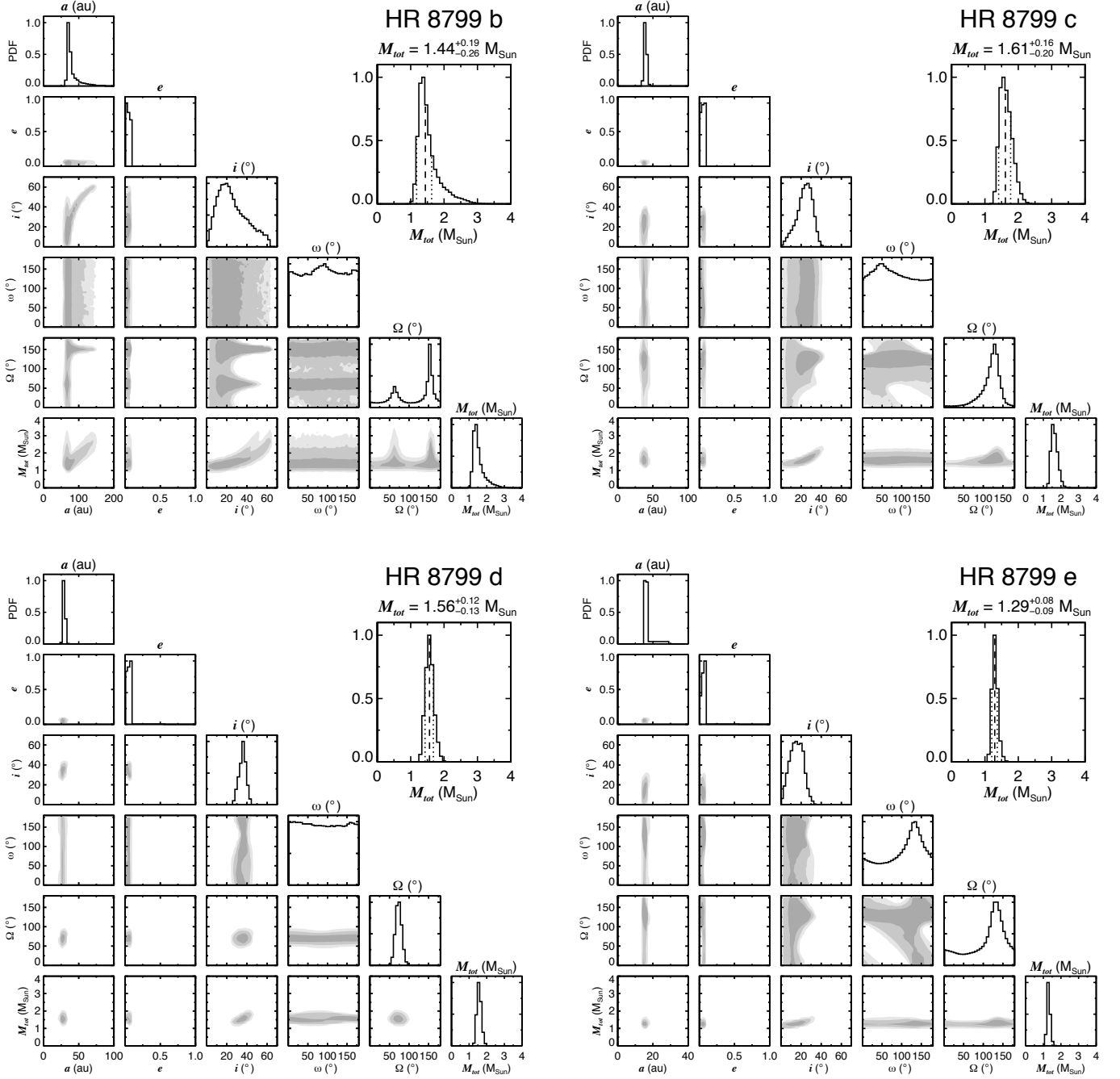


Figure 9. Same as Figure 8 but for the low eccentricity scenario as described in §4.1.

Table 5. HR 8799 Orbit Fit Results (Low-Eccentricity Scenario)

Parameter	Median	MAP ^a	68.3% CI	95.4% CI
HR 8799 b				
a (AU)	73.8	70.5	(65.6, 79.5)	(64.1, 121)
e	0.044	0.0	(0.0, 0.063)	(0.0, 0.094)
i ($^{\circ}$)	23	19	(6.4, 34)	(3, 56)
ω ($^{\circ}$)	90	95	(60, 180)	(7.4, 179)
Ω ($^{\circ}$)	136	154	(62, 161)	(19, 180)
M_{tot} (M_{\odot})	1.44	1.35	(1.18, 1.63)	(1.1, 2.31)
HR 8799 c				
a (AU)	39.3	39.5	(37.4, 40.9)	(36.1, 42.7)
e	0.053	0.06	(0.034, 0.10)	(0.0, 0.10)
i ($^{\circ}$)	24	26	(18, 33)	(7, 37)
ω ($^{\circ}$)	83	50	(1.5, 118)	(1, 172)
Ω ($^{\circ}$)	124	131	(110, 145)	(52, 167)
M_{tot} (M_{\odot})	1.61	1.51	(1.41, 1.77)	(1.31, 2.01)
HR 8799 d				
a (AU)	29.2	29.5	(27.8, 30.5)	(26.6, 32.1)
e	0.053	0.095	(0.034, 0.10)	(0.0, 0.10)
i ($^{\circ}$)	36	36	(32, 39)	(30, 42)
ω ($^{\circ}$)	88.9	17.5	(0.00841, 123)	(0.036, 172)
Ω ($^{\circ}$)	73.1	73	(65, 80.9)	(58, 88.9)
M_{tot} (M_{\odot})	1.56	1.57	(1.43, 1.68)	(1.3, 1.82)
HR 8799 e				
a (AU)	16.0	15.5	(15.4, 16.5)	(14.9, 17.1)
e	0.063	0.06	(0.048, 0.10)	(0.0, 0.10)
i ($^{\circ}$)	16	14	(9.1, 23)	(3, 27)
ω ($^{\circ}$)	115	130	(82, 180)	(10, 180)
Ω ($^{\circ}$)	120	130	(96, 174)	(13, 180)
M_{tot} (M_{\odot})	1.29	1.29	(1.21, 1.37)	(1.14, 1.48)

^aMaximum a posteriori probability.

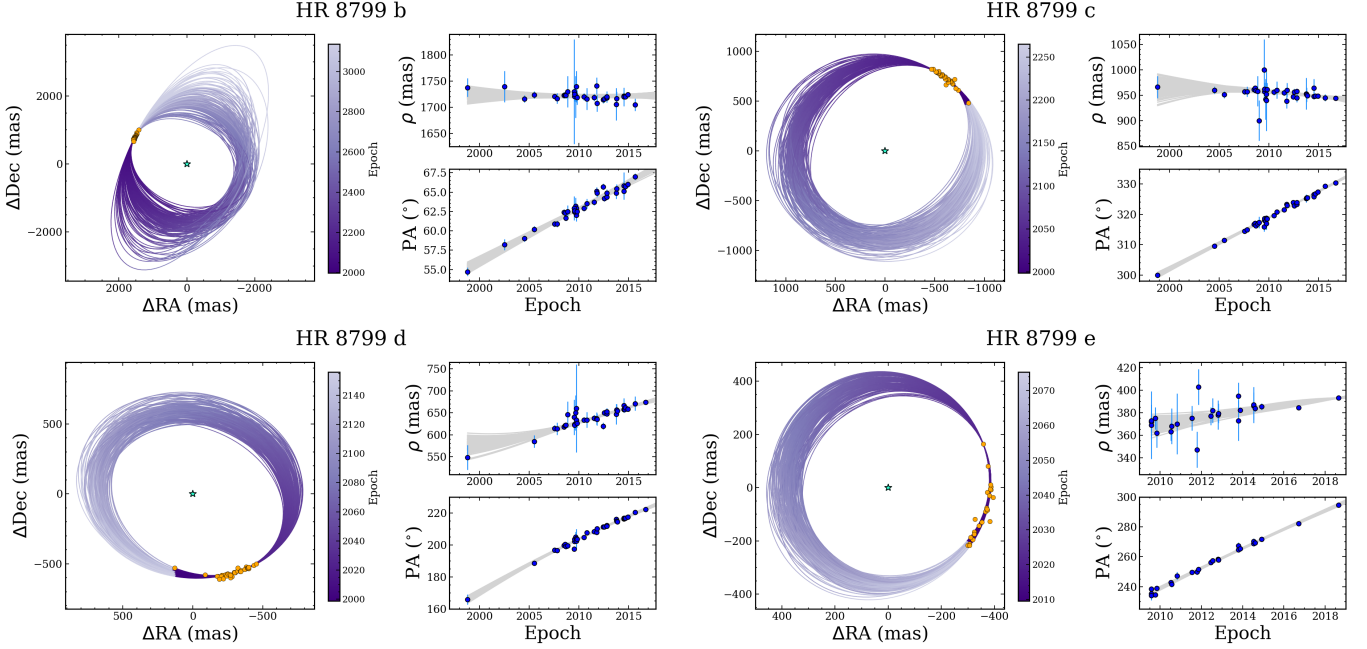


Figure 10. Same as Figure 4 but for the low-eccentricity scenario as described in §4.1.

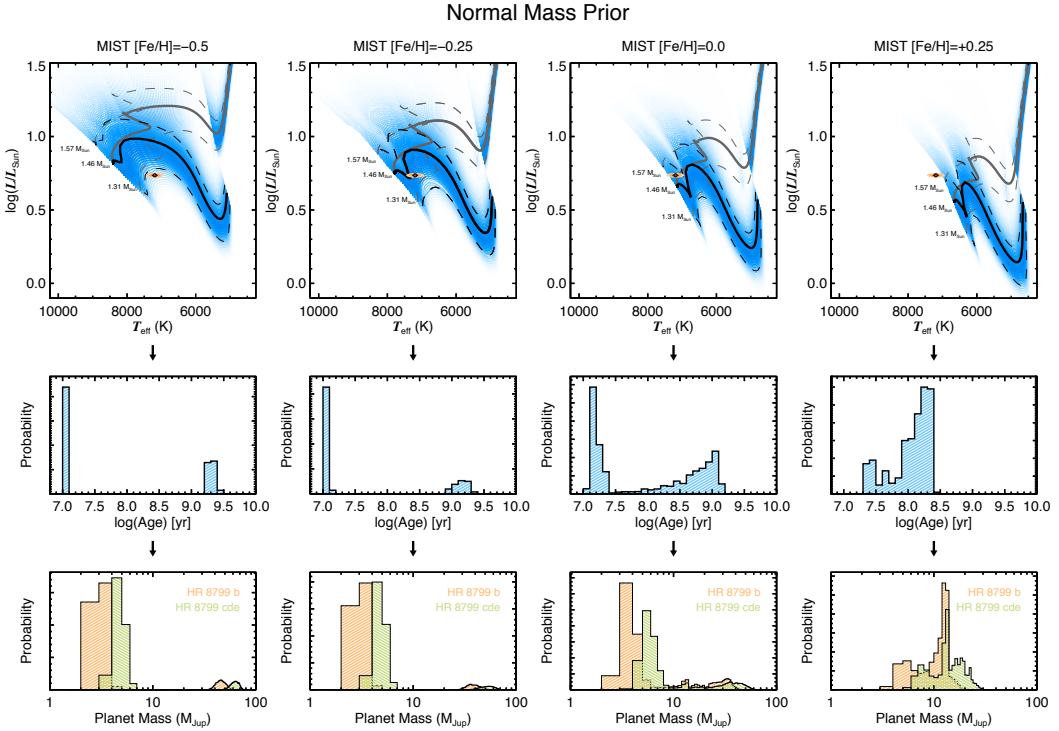


Figure 11. Same as Figure 7 but using the dynamical mass with an informed Gaussian prior of $1.47 \pm 0.30 M_{\odot}$ for the stellar mass.

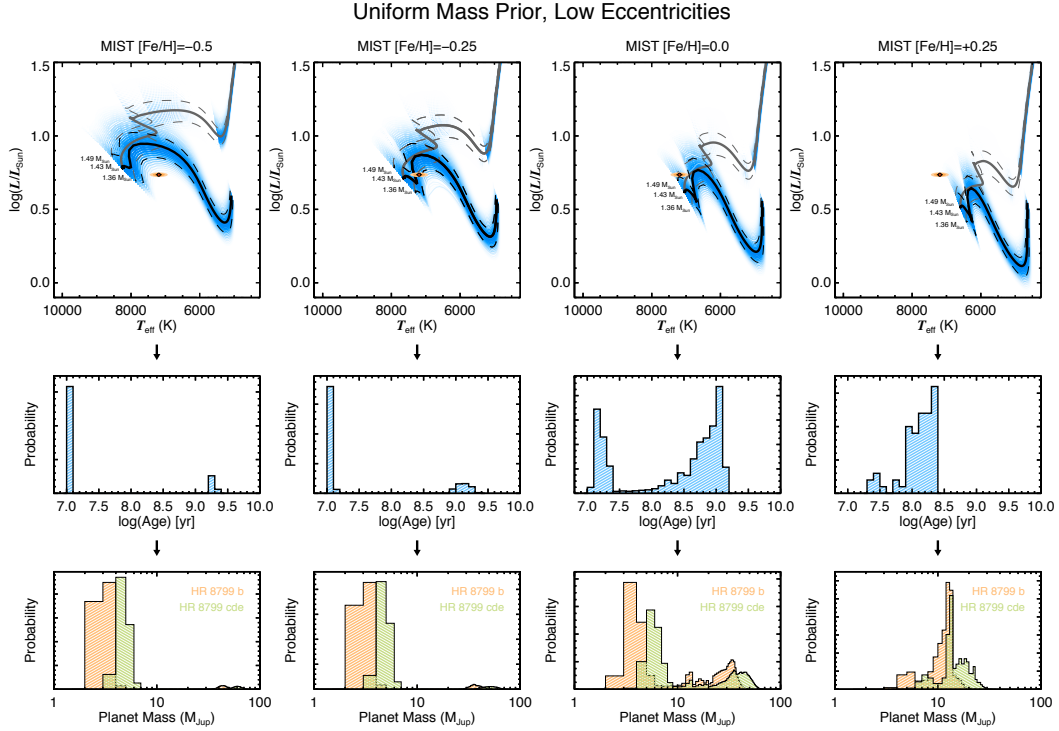


Figure 12. Same as Figure 7 but using the dynamical mass with a uniform prior and low eccentricities.

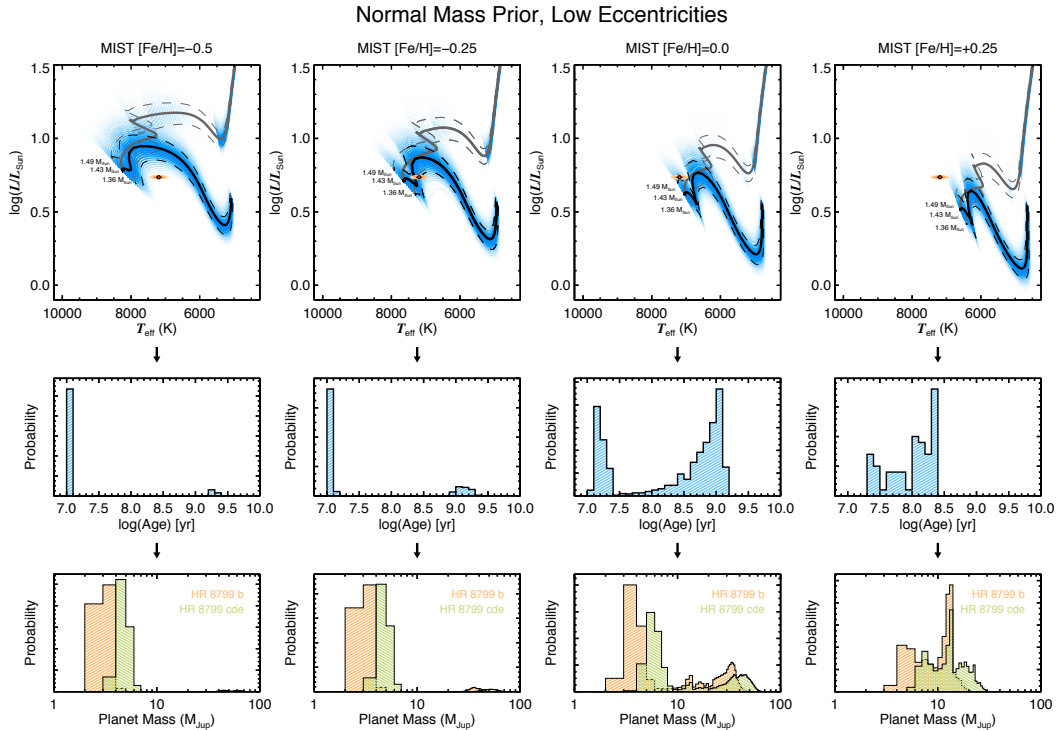


Figure 13. Same as Figure 7 but using the dynamical mass with an informed Gaussian prior of $1.47 \pm 0.30 M_{\odot}$ for the stellar mass and low eccentricities.

REFERENCES

Apai, D., Kasper, M., Skemer, A., et al. 2016, *ApJ*, 820, 40, doi: [10.3847/0004-637X/820/1/40](https://doi.org/10.3847/0004-637X/820/1/40)

Astropy Collaboration, Robitaille, T. P., Tollerud, E. J., et al. 2013, *A&A*, 558, A33, doi: [10.1051/0004-6361/201322068](https://doi.org/10.1051/0004-6361/201322068)

Astropy Collaboration, Price-Whelan, A. M., Sipőcz, B. M., et al. 2018, *AJ*, 156, 123, doi: [10.3847/1538-3881/aabc4f](https://doi.org/10.3847/1538-3881/aabc4f)

Baines, E. K., White, R. J., Huber, D., et al. 2012, *ApJ*, 761, 57, doi: [10.1088/0004-637X/761/1/57](https://doi.org/10.1088/0004-637X/761/1/57)

Bell, C. P. M., Mamajek, E. E., & Naylor, T. 2015, *MNRAS*, 454, 593, doi: [10.1093/mnras/stv1981](https://doi.org/10.1093/mnras/stv1981)

Biller, B. A., Apai, D., Bonnefoy, M., et al. 2021, *MNRAS*, 503, 743, doi: [10.1093/mnras/stab202](https://doi.org/10.1093/mnras/stab202)

Blunt, S., Wang, J. J., Angelo, I., et al. 2020, *AJ*, 159, 89, doi: [10.3847/1538-3881/ab6663](https://doi.org/10.3847/1538-3881/ab6663)

Bohn, A. J., Kenworthy, M. A., Ginski, C., et al. 2020a, *MNRAS*, 492, 431, doi: [10.1093/mnras/stz3462](https://doi.org/10.1093/mnras/stz3462)

—. 2020b, *ApJL*, 898, L16, doi: [10.3847/2041-8213/aba27e](https://doi.org/10.3847/2041-8213/aba27e)

Booth, M., Jordán, A., Casassus, S., et al. 2016, *MNRAS*, 460, L10, doi: [10.1093/mnrasl/slw040](https://doi.org/10.1093/mnrasl/slw040)

Bowler, B. P. 2016, *PASP*, 128, 102001, doi: [10.1088/1538-3873/128/968/102001](https://doi.org/10.1088/1538-3873/128/968/102001)

Bowler, B. P., Blunt, S. C., & Nielsen, E. L. 2020, *AJ*, 159, 63, doi: [10.3847/1538-3881/ab5b11](https://doi.org/10.3847/1538-3881/ab5b11)

Bowler, B. P., Liu, M. C., Shkolnik, E. L., & Tamura, M. 2015, *ApJS*, 216, 7

Bowler, B. P., Dupuy, T. J., Endl, M., et al. 2018, *AJ*, 155, 159

Boyajian, T. S., von Braun, K., van Belle, G., et al. 2013, *ApJ*, 771, 40, doi: [10.1088/0004-637X/771/1/40](https://doi.org/10.1088/0004-637X/771/1/40)

Brandt, G. M., Brandt, T. D., Dupuy, T. J., Li, Y., & Michalik, D. 2021a, *AJ*, 161, 179, doi: [10.3847/1538-3881/abdc2e](https://doi.org/10.3847/1538-3881/abdc2e)

Brandt, G. M., Brandt, T. D., Dupuy, T. J., Michalik, D., & Marleau, G.-D. 2021b, *ApJL*, 915, L16, doi: [10.3847/2041-8213/ac0540](https://doi.org/10.3847/2041-8213/ac0540)

Burrows, A., Marley, M., Hubbard, W. B., et al. 1997, *ApJ*, 491, 856, doi: [10.1086/305002](https://doi.org/10.1086/305002)

Choi, J., Dotter, A., Conroy, C., et al. 2016, *ApJ*, 823, 102, doi: [10.3847/0004-637X/823/2/102](https://doi.org/10.3847/0004-637X/823/2/102)

Currie, T., Fukagawa, M., Thalmann, C., Matsumura, S., & Plavchan, P. 2012, *ApJL*, 755, L34, doi: [10.1088/2041-8205/755/2/L34](https://doi.org/10.1088/2041-8205/755/2/L34)

Currie, T., Burrows, A., Itoh, Y., et al. 2011, *ApJ*, 729, 128, doi: [10.1088/0004-637X/729/2/128](https://doi.org/10.1088/0004-637X/729/2/128)

Currie, T., Burrows, A., Girard, J. H., et al. 2014, *ApJ*, 795, 133, doi: [10.1088/0004-637X/795/2/133](https://doi.org/10.1088/0004-637X/795/2/133)

De Rosa, R. J., Nguyen, M. M., Chilcote, J., et al. 2020, *Journal of Astronomical Telescopes, Instruments, and Systems*, 6, 015006, doi: [10.1117/1.JATIS.6.1.015006](https://doi.org/10.1117/1.JATIS.6.1.015006)

Dotter, A. 2016, *ApJS*, 222, 8, doi: [10.3847/0067-0049/222/1/8](https://doi.org/10.3847/0067-0049/222/1/8)

Doyon, R., Lafrenière, D., Artigau, E., Malo, L., & Marois, C. 2010, in *In the Spirit of Lyot* 2010, E42

Dupuy, T. J., Brandt, T. D., Kratter, K. M., & Bowler, B. P. 2019, *ApJL*, 871, L4, doi: [10.3847/2041-8213/aafb31](https://doi.org/10.3847/2041-8213/aafb31)

Esposito, S., Mesa, D., Skemer, A., et al. 2013, *A&A*, 549, A52, doi: [10.1051/0004-6361/201219212](https://doi.org/10.1051/0004-6361/201219212)

Fabrycky, D. C., & Murray-Clay, R. A. 2010, *ApJ*, 710, 1408, doi: [10.1088/0004-637X/710/2/1408](https://doi.org/10.1088/0004-637X/710/2/1408)

Faramaz, V., Marino, S., Booth, M., et al. 2021, *AJ*, 161, 271, doi: [10.3847/1538-3881/abf4e0](https://doi.org/10.3847/1538-3881/abf4e0)

Foreman-Mackey, D., Hogg, D. W., Lang, D., & Goodman, J. 2013, *PASP*, 125, 306, doi: [10.1086/670067](https://doi.org/10.1086/670067)

Fortney, J. J., Marley, M. S., Saumon, D., & Lodders, K. 2008, *ApJ*, 683, 1104, doi: [10.1086/589942](https://doi.org/10.1086/589942)

Gagné, J., Mamajek, E. E., Malo, L., et al. 2018, *ApJ*, 856, 23, doi: [10.3847/1538-4357/aaae09](https://doi.org/10.3847/1538-4357/aaae09)

Gaia Collaboration, Prusti, T., de Bruijne, J. H. J., et al. 2016, *A&A*, 595, A1, doi: [10.1051/0004-6361/201629272](https://doi.org/10.1051/0004-6361/201629272)

Gaia Collaboration, Brown, A. G. A., Vallenari, A., et al. 2021, *A&A*, 649, A1, doi: [10.1051/0004-6361/202039657](https://doi.org/10.1051/0004-6361/202039657)

Galicher, R., Marois, C., Macintosh, B., Barman, T., & Konopacky, Q. 2011, *ApJL*, 739, L41, doi: [10.1088/2041-8205/739/2/L41](https://doi.org/10.1088/2041-8205/739/2/L41)

Goodman, J., & Weare, J. 2010, *Communications in Applied Mathematics and Computational Science*, Vol. 5, No. 1, p. 65-80, 2010, 5, 65, doi: [10.2140/camcos.2010.5.65](https://doi.org/10.2140/camcos.2010.5.65)

Goździewski, K., & Migaszewski, C. 2014, *MNRAS*, 440, 3140, doi: [10.1093/mnras/stu455](https://doi.org/10.1093/mnras/stu455)

—. 2018, *ApJS*, 238, 6, doi: [10.3847/1538-4365/aad3d3](https://doi.org/10.3847/1538-4365/aad3d3)

—. 2020, *ApJL*, 902, L40, doi: [10.3847/2041-8213/abb881](https://doi.org/10.3847/2041-8213/abb881)

Gravity Collaboration, Lacour, S., Nowak, M., et al. 2019, *A&A*, 623, L11, doi: [10.1051/0004-6361/201935253](https://doi.org/10.1051/0004-6361/201935253)

Gravity Collaboration, Nowak, M., Lacour, S., et al. 2020, *A&A*, 633, A110, doi: [10.1051/0004-6361/201936898](https://doi.org/10.1051/0004-6361/201936898)

Gray, R. O., & Kaye, A. B. 1999, *AJ*, 118, 2993, doi: [10.1086/301134](https://doi.org/10.1086/301134)

Greenbaum, A. Z., Pueyo, L., Ruffio, J.-B., et al. 2018, *AJ*, 155, 226, doi: [10.3847/1538-3881/aabcb8](https://doi.org/10.3847/1538-3881/aabcb8)

Haffert, S. Y., Bohn, A. J., de Boer, J., et al. 2019, *Nature Astronomy*, 3, 749, doi: [10.1038/s41550-019-0780-5](https://doi.org/10.1038/s41550-019-0780-5)

Harris, C. R., Millman, K. J., van der Walt, S. J., et al. 2020, *Nature*, 585, 357, doi: [10.1038/s41586-020-2649-2](https://doi.org/10.1038/s41586-020-2649-2)

Hillenbrand, L. A., & White, R. J. 2004, *ApJ*, 604, 741, doi: [10.1086/382021](https://doi.org/10.1086/382021)

Hinz, P. M., Rodigas, T. J., Kenworthy, M. A., et al. 2010, *ApJ*, 716, 417, doi: [10.1088/0004-637X/716/1/417](https://doi.org/10.1088/0004-637X/716/1/417)

Hunter, J. D. 2007, *Computing in Science Engineering*, 9, 90, doi: [10.1109/MCSE.2007.55](https://doi.org/10.1109/MCSE.2007.55)

Kaye, A. B., Handler, G., Krisciunas, K., Poretti, E., & Zerbi, F. M. 1999, *PASP*, 111, 840, doi: [10.1086/316399](https://doi.org/10.1086/316399)

Keppler, M., Benisty, M., Müller, A., et al. 2018, *A&A*, 617, A44, doi: [10.1051/0004-6361/201832957](https://doi.org/10.1051/0004-6361/201832957)

Konopacky, Q. M., & Barman, T. S. 2018, *HR8799: Imaging a System of Exoplanets*, ed. H. J. Deeg & J. A. Belmonte, 36, doi: [10.1007/978-3-319-55333-7_36](https://doi.org/10.1007/978-3-319-55333-7_36)

Konopacky, Q. M., Marois, C., Macintosh, B. A., et al. 2016, *AJ*, 152, 28, doi: [10.3847/0004-6256/152/2/28](https://doi.org/10.3847/0004-6256/152/2/28)

Lacour, S., Wang, J. J., Rodet, L., et al. 2021, *A&A*, 654, L2, doi: [10.1051/0004-6361/202141889](https://doi.org/10.1051/0004-6361/202141889)

Lafrenière, D., Marois, C., Doyon, R., & Barman, T. 2009, *ApJL*, 694, L148, doi: [10.1088/0004-637X/694/2/L148](https://doi.org/10.1088/0004-637X/694/2/L148)

Lafrenière, D., Marois, C., Doyon, R., Nadeau, D., & Artigau, É. 2007, *ApJ*, 660, 770

Lagrange, A. M., Gratadour, D., Chauvin, G., et al. 2009, *A&A*, 493, L21, doi: [10.1051/0004-6361:200811325](https://doi.org/10.1051/0004-6361:200811325)

Lagrange, A. M., Bonnefoy, M., Chauvin, G., et al. 2010, *Science*, 329, 57, doi: [10.1126/science.1187187](https://doi.org/10.1126/science.1187187)

Lagrange, A. M., Meunier, N., Rubini, P., et al. 2019, *Nature Astronomy*, 3, 1135, doi: [10.1038/s41550-019-0857-1](https://doi.org/10.1038/s41550-019-0857-1)

Lagrange, A. M., Rubini, P., Nowak, M., et al. 2020, *A&A*, 642, A18, doi: [10.1051/0004-6361/202038823](https://doi.org/10.1051/0004-6361/202038823)

Lindegren, L., Bastian, U., Biermann, M., et al. 2021, *A&A*, 649, A4, doi: [10.1051/0004-6361/202039653](https://doi.org/10.1051/0004-6361/202039653)

Liu, M. C. 2004, *Science*, 305, 1442, doi: [10.1126/science.1102929](https://doi.org/10.1126/science.1102929)

Maire, A.-L., Skemer, A. J., Hinz, P. M., et al. 2015, *A&A*, 576, A133, doi: [10.1051/0004-6361/201425185](https://doi.org/10.1051/0004-6361/201425185)

Malo, L., Doyon, R., Lafrenière, D., et al. 2013, *ApJ*, 762, 88, doi: [10.1088/0004-637X/762/2/88](https://doi.org/10.1088/0004-637X/762/2/88)

Marleau, G.-D., & Cumming, A. 2014, *MNRAS*, 437, 1378, doi: [10.1093/mnras/stt1967](https://doi.org/10.1093/mnras/stt1967)

Marley, M. S., Fortney, J. J., Hubickyj, O., Bodenheimer, P., & Lissauer, J. J. 2007, *ApJ*, 655, 541, doi: [10.1086/509759](https://doi.org/10.1086/509759)

Marois, C., Lafrenière, D., Doyon, R., Macintosh, B., & Nadeau, D. 2006, *ApJ*, 641, 556

Marois, C., Macintosh, B., Barman, T., et al. 2008, *Science*, 322, 1348, doi: [10.1126/science.1166585](https://doi.org/10.1126/science.1166585)

Marois, C., Zuckerman, B., Konopacky, Q. M., Macintosh, B., & Barman, T. 2010, *Nature*, 468, 1080, doi: [10.1038/nature09684](https://doi.org/10.1038/nature09684)

Mesa, D., Keppler, M., Cantalloube, F., et al. 2019, *A&A*, 632, A25, doi: [10.1051/0004-6361/201936764](https://doi.org/10.1051/0004-6361/201936764)

Metchev, S., Marois, C., & Zuckerman, B. 2009, *ApJL*, 705, L204, doi: [10.1088/0004-637X/705/2/L204](https://doi.org/10.1088/0004-637X/705/2/L204)

Moya, A., Amado, P. J., Barrado, D., et al. 2010a, *MNRAS*, 405, L81, doi: [10.1111/j.1745-3933.2010.00863.x](https://doi.org/10.1111/j.1745-3933.2010.00863.x)

—. 2010b, *MNRAS*, 406, 566, doi: [10.1111/j.1365-2966.2010.16699.x](https://doi.org/10.1111/j.1365-2966.2010.16699.x)

Murphy, S. J., Joyce, M., Bedding, T. R., White, T. R., & Kama, M. 2021, *MNRAS*, 502, 1633, doi: [10.1093/mnras/stab144](https://doi.org/10.1093/mnras/stab144)

Murphy, S. J., Corbally, C. J., Gray, R. O., et al. 2015, *PASA*, 32, e036, doi: [10.1017/pasa.2015.34](https://doi.org/10.1017/pasa.2015.34)

Nelder, J. A., & Mead, R. 1965, *The Computer Journal*, 7, 308

Nielsen, E. L., Liu, M. C., Wahhaj, Z., et al. 2014, *ApJ*, 794, 158, doi: [10.1088/0004-637X/794/2/158](https://doi.org/10.1088/0004-637X/794/2/158)

Nielsen, E. L., De Rosa, R. J., Wang, J. J., et al. 2020, *AJ*, 159, 71, doi: [10.3847/1538-3881/ab5b92](https://doi.org/10.3847/1538-3881/ab5b92)

Nowak, M., Lacour, S., Lagrange, A. M., et al. 2020, *A&A*, 642, L2, doi: [10.1051/0004-6361/202039039](https://doi.org/10.1051/0004-6361/202039039)

Paxton, B., Bildsten, L., Dotter, A., et al. 2011, *ApJS*, 192, 3, doi: [10.1088/0067-0049/192/1/3](https://doi.org/10.1088/0067-0049/192/1/3)

Paxton, B., Cantiello, M., Arras, P., et al. 2013, *ApJS*, 208, 4, doi: [10.1088/0067-0049/208/1/4](https://doi.org/10.1088/0067-0049/208/1/4)

Paxton, B., Marchant, P., Schwab, J., et al. 2015, *ApJS*, 220, 15, doi: [10.1088/0067-0049/220/1/15](https://doi.org/10.1088/0067-0049/220/1/15)

Paxton, B., Schwab, J., Bauer, E. B., et al. 2018, *ApJS*, 234, 34, doi: [10.3847/1538-4365/aaa5a8](https://doi.org/10.3847/1538-4365/aaa5a8)

Pueyo, L., Soummer, R., Hoffmann, J., et al. 2015, *ApJ*, 803, 31, doi: [10.1088/0004-637X/803/1/31](https://doi.org/10.1088/0004-637X/803/1/31)

Rajan, A., Barman, T., Soummer, R., et al. 2015, *ApJL*, 809, L33, doi: [10.1088/2041-8205/809/2/L33](https://doi.org/10.1088/2041-8205/809/2/L33)

Rodriguez, E., & Zerbi, F. M. 1995, *Information Bulletin on Variable Stars*, 4170, 1

Ruffio, J.-B., Macintosh, B., Konopacky, Q. M., et al. 2019, *AJ*, 158, 200, doi: [10.3847/1538-3881/ab4594](https://doi.org/10.3847/1538-3881/ab4594)

Ruffio, J.-B., Konopacky, Q. M., Barman, T., et al. 2021, arXiv e-prints, arXiv:2109.07614. <https://arxiv.org/abs/2109.07614>

Sadakane, K. 2006, *PASJ*, 58, 1023, doi: [10.1093/pasj/58.6.1023](https://doi.org/10.1093/pasj/58.6.1023)

Serenelli, A., Weiss, A., Aerts, C., et al. 2021, *A&A Rv*, 29, 4, doi: [10.1007/s00159-021-00132-9](https://doi.org/10.1007/s00159-021-00132-9)

Service, M., Lu, J. R., Campbell, R., et al. 2016, *PASP*, 128, 095004

Sódor, Á., Chené, A. N., De Cat, P., et al. 2014, *A&A*, 568, A106, doi: [10.1051/0004-6361/201423976](https://doi.org/10.1051/0004-6361/201423976)

Soummer, R., Hagan, J. B., Pueyo, L., et al. 2011, *ApJ*, 741, 55, doi: [10.1088/0004-637X/741/1/55](https://doi.org/10.1088/0004-637X/741/1/55)

Su, K. Y. L., Rieke, G. H., Stapelfeldt, K. R., et al. 2009, *ApJ*, 705, 314, doi: [10.1088/0004-637X/705/1/314](https://doi.org/10.1088/0004-637X/705/1/314)

van der Walt, S., Colbert, S. C., & Varoquaux, G. 2011, Computing in Science and Engineering, 13, 22, doi: [10.1109/MCSE.2011.37](https://doi.org/10.1109/MCSE.2011.37)

van Leeuwen, F. 2007, *A&A*, 474, 653, doi: [10.1051/0004-6361:20078357](https://doi.org/10.1051/0004-6361:20078357)

Vandal, T., Rameau, J., & Doyon, R. 2020, *AJ*, 160, 243, doi: [10.3847/1538-3881/abba30](https://doi.org/10.3847/1538-3881/abba30)

Veras, D., & Hinkley, S. 2021, *MNRAS*, 505, 1557, doi: [10.1093/mnras/stab1311](https://doi.org/10.1093/mnras/stab1311)

Vousden, W. D., Farr, W. M., & Mandel, I. 2016, *MNRAS*, 455, 1919, doi: [10.1093/mnras/stv2422](https://doi.org/10.1093/mnras/stv2422)

Wahhaj, Z., Milli, J., Romero, C., et al. 2021, *A&A*, 648, A26, doi: [10.1051/0004-6361/202038794](https://doi.org/10.1051/0004-6361/202038794)

Wang, J., Mawet, D., Fortney, J. J., et al. 2018a, *AJ*, 156, 272, doi: [10.3847/1538-3881/aae47b](https://doi.org/10.3847/1538-3881/aae47b)

Wang, J. J., Graham, J. R., Pueyo, L., et al. 2016, *AJ*, 152, 97, doi: [10.3847/0004-6256/152/4/97](https://doi.org/10.3847/0004-6256/152/4/97)

Wang, J. J., Graham, J. R., Dawson, R., et al. 2018b, *AJ*, 156, 192, doi: [10.3847/1538-3881/aae150](https://doi.org/10.3847/1538-3881/aae150)

Wang, J. J., Ruffio, J.-B., Morris, E., et al. 2021, *AJ*, 162, 148, doi: [10.3847/1538-3881/ac1349](https://doi.org/10.3847/1538-3881/ac1349)

Wertz, O., Absil, O., Gómez González, C. A., et al. 2017, *A&A*, 598, A83, doi: [10.1051/0004-6361/201628730](https://doi.org/10.1051/0004-6361/201628730)

Wilner, D. J., MacGregor, M. A., Andrews, S. M., et al. 2018, *ApJ*, 855, 56, doi: [10.3847/1538-4357/aaacd7](https://doi.org/10.3847/1538-4357/aaacd7)

Wizinowich, P. 2013, *PASP*, 125, 798

Wright, D. J., Chené, A. N., De Cat, P., et al. 2011, *ApJL*, 728, L20, doi: [10.1088/2041-8205/728/1/L20](https://doi.org/10.1088/2041-8205/728/1/L20)

Yi, S., Demarque, P., Kim, Y.-C., et al. 2001, *ApJS*, 136, 417, doi: [10.1086/321795](https://doi.org/10.1086/321795)

Zerbi, F. M., Rodríguez, E., Garrido, R., et al. 1999, *MNRAS*, 303, 275, doi: [10.1046/j.1365-8711.1999.02209.x](https://doi.org/10.1046/j.1365-8711.1999.02209.x)

Zuckerman, B., Rhee, J. H., Song, I., & Bessell, M. S. 2011, *ApJ*, 732, 61, doi: [10.1088/0004-637X/732/2/61](https://doi.org/10.1088/0004-637X/732/2/61)

Zurlo, A., Vigan, A., Galicher, R., et al. 2016, *A&A*, 587, A57, doi: [10.1051/0004-6361/201526835](https://doi.org/10.1051/0004-6361/201526835)